BNL-106289-2014-JA

AGU PUBLICATIONS

JGR

Journal of Geophysical Research: Atmospheres

RESEARCH ARTICLE
10.1002/2014JD022011

Special Section:
Fast Physics in Climate Models: Parameterization, Evaluation and Observation

Key Points:
- Elevated storms and squall lines occur in very different environments
- Squall lines show much stronger heating than the elevated storms

Correspondence to:
S. Xie,
xie2@llnl

Citation:
Xie, S., Y. Zhang, S. E. Giangrande, M. P. Jensen, R. McCoy, and M. Zhang (2014), Interactions between cumulus convection and its environment as revealed by the MC3E sounding array, *J. Geophys. Res. Atmos.*, *119*, 11,784–11,808, doi:10.1002/2014JD022011.

Received 8 MAY 2014
Accepted 27 SEP 2014
Accepted article online 1 OCT 2014
Published online 31 OCT 2014

Interactions between cumulus convection and its environment as revealed by the MC3E sounding array

Shaocheng Xie[1], Yunyan Zhang[1], Scott E. Giangrande[2], Michael P. Jensen[2], Renata McCoy[1], and Minghua Zhang[3]

[1]Lawrence Livermore National Laboratory, Livermore, California, USA, [2]Brookhaven National Laboratory, Upton, New York, USA, [3]School of Marine and Atmospheric Sciences, Stony Brook University, Stony Brook, New York, USA

Abstract This study attempts to understand interactions between midlatitude convective systems and their environments through a heat and moisture budget analysis using the sounding data collected from the Midlatitude Continental Convective Clouds Experiment (MC3E) in central Oklahoma. Distinct large-scale structures and diabatic heating and drying profiles are presented for cases of weaker and elevated thunderstorms as well as intense squall line and supercell thunderstorm events during the campaign. The elevated cell events were nocturnal convective systems occurring in an environment having low convective available potential energy (CAPE) and a very dry boundary layer. In contrast, deeper convective events happened during the morning into early afternoon within an environment associated with large CAPE and a near-saturated boundary layer. As the systems reached maturity, the diagnosed diabatic heating in the latter deep convective cases was much stronger and of greater vertical extent than the former. Both groups showed considerable diabatic cooling in the lower troposphere, associated with the evaporation of precipitation and low-level clouds. The horizontal advection of moisture also played a dominant role in moistening the lower troposphere, particularly for the deeper convective events, wherein the near surface southeasterly flow allows persistent low-level moisture return from the Gulf of Mexico to support convection. The moisture convergence often was present before these systems develop, suggesting a strong correlation between the large-scale moisture convergence and convection. Sensitivity tests indicated that the uncertainty in the surface precipitation and the size of analysis domain mainly affected the magnitude of these analyzed fields rather than their vertical structures.

1. Introduction

After decades of effort, accurately representing cumulus convection is still one of the most challenging tasks for weather and climate modeling. This is primarily because the interaction between cumulus convection and its environment has not been fully understood. In general, the large-scale state of the atmosphere, as characterized by low-level convergence and moistening and middle and upper level advective cooling, acts to destabilize the atmospheric structure, thereby initiating and maintaining convection. On the other hand, cumulus clouds modify the temperature and moisture structure of the environment through the release of latent heat and the vertical redistribution of sensible heat and water vapor [*Riehl and Malkus*, 1958; *Yanai*, 1961; *Yanai and Johnson*, 1993]. However, the details of these interactions may differ, depending on the large-scale conditions and vertical structures of diabatic heating and drying. These interactions also may vary according to the temporal and spatial scales of interest.

Collecting the observational data necessary to diagnose vertical structures of latent heating and the drying associated with convective systems has been a primary goal for numerous major field experiments [e.g., *Webster and Lukas*, 1992; *May et al*., 2008; *Zhang et al*., 2013]. During convective periods, latent heating is the dominant component of total diabatic heating. The total diabatic heating and drying, jointly termed as the apparent heat source (Q_1) and apparent moisture sink (Q_2) according to *Yanai et al*. [1973], can be estimated as the residual of heat and moisture budgets of large-scale motion measured by a suitably designed sounding network [e.g., *Yanai et al*., 1973; *Thompson et al*., 1979; *Ooyama*, 1987; *Zhang and Lin*, 1997]. Previous budget diagnostic studies have often targeted tropical convective systems given the dominant role these convective systems play in the global water cycle [*Thompson et al*., 1979; *Frank*, 1978; *Frank and McBride*,

1989; *Lin and Johnson*, 1996a, 1996b; *Schumacher et al*., 2007; *Xie et al*., 2010a; *Johnson and Ciesielski*, 2013]. Few suitably designed field studies have been carried out in the midlatitudes [*Ninomiya*, 1971; *Lewis*, 1975; *Kuo and Anthes*, 1984; *Gallus and Johnson*, 1995; *Hopper and Schumacher*, 2009; *Hopper and Schumacher*, 2011].

Convection in the midlatitudes often occurs less frequent as compared to tropical counterparts. The low frequency of midlatitude convective events implies that the overall impact of diabatic heating to the large-scale environment is small compared to the tropics, but to the maintenance of the storms itself, it may be important. For example, the strong cooling due to drier lower troposphere will create stronger cold pools, which will have feedbacks to the storm (especially squall line) to sustain it while propagating. In addition, groups of mesoscale convective systems that often occur in the midlatitude over a several-day period in the summer can have large impact on the large-scale flow patterns [*Stensrud*, 1996]. To provide a more comprehensive data set to better characterize convection and its environment in the midlatitudes, a major field campaign, the Midlatitude Continental Convective Clouds Experiment (MC3E) [*Jensen et al*., 2010] was recently conducted from 22 April to 6 June 2011 at the Atmospheric Radiation Measurement (ARM) Southern Great Plains (SGP) site in central Oklahoma. This campaign was funded through a collaborative effect between the U.S. Department of Energy (DOE) ARM program and the National Aeronautic and Space Administration's Global Precipitation Measurement mission Ground Validation program. It leveraged the largest observing infrastructure currently available in the central United States to observe the detailed evolution of convective cloud systems and their large-scale conditions. A key component for this experiment included extensive radiosonde launches at 3–6 h intervals over a distributed network of six sounding stations to capture the diurnal variability of convective cloud systems whenever they propagated over the SGP site. The data set collected from this experiment and anchored by this extensive sounding array provided a unique opportunity to study the structure and evolution of these midlatitude convective systems and their associated environments at an unprecedented level of detail.

The goal of this study is to improve our understanding on the interactions between cumulus convection and its environment in midlatitude convective cloud systems using the unique data collected during MC3E. We include a comparison of well-organized squall lines and deeper convective systems with nocturnal weaker and elevated convective episodes over the ARM SGP location during the campaign. These are two typical convective systems that are often observed in this region. Using these unique MC3E sounding data constrained with surface and top-of-the-atmosphere (TOA) measurements through a variational analysis method, we compute the large-scale budgets of temperature and moisture, then estimate the total diabatic heating and drying structures in these convective systems. Our focus is to define similarities and variations in large-scale conditions as well as diabatic heating and drying structures for the two different bulk convective cloud system types. We attempt to understand how the large-scale atmospheric structure interacts with these convective systems under different conditions. An important end product of this study is the analyzed large-scale vertical velocity and advective tendencies of temperature and moisture, which can be used to drive single-column models and cloud-resolving models for modeling study of these observed MC3E cloud systems [e.g., *Ghan et al*., 2000; *Xie et al*., 2002, 2005; *Xu et al*., 2002, 2005].

Details about the objective analysis method used in the budget analysis are provided in section 2. Section 3 presents an overview of the observed convective systems and their environments. The analyzed heat and moisture budgets are discussed in section 4. The discussion focuses on the similarities and differences in the budget terms and their large-scale structures between the examined weaker discrete and/or elevated thunderstorms and the intense squall line and supercell events. Section 5 analyzes impacts of uncertainties in the surface precipitation on the derived heat and moisture budgets, as well as how the heat and moisture budgets vary with different analysis domain sizes. Section 6 provides a summary of the study.

2. Analysis Method

The method used to compute heat and moisture budgets is the constrained objective variational analysis approach of *Zhang and Lin* [1997]. This method was designed for deriving the large-scale vertical velocity and advective tendencies of temperature and moisture, the so-called large-scale forcing, from sounding measurements over a network with a small number of stations. Compared to other conventional objective analysis methods, the unique feature of the variational analysis is the use of domain-averaged surface and TOA observations as constraints to adjust atmospheric state variables from soundings by the smallest

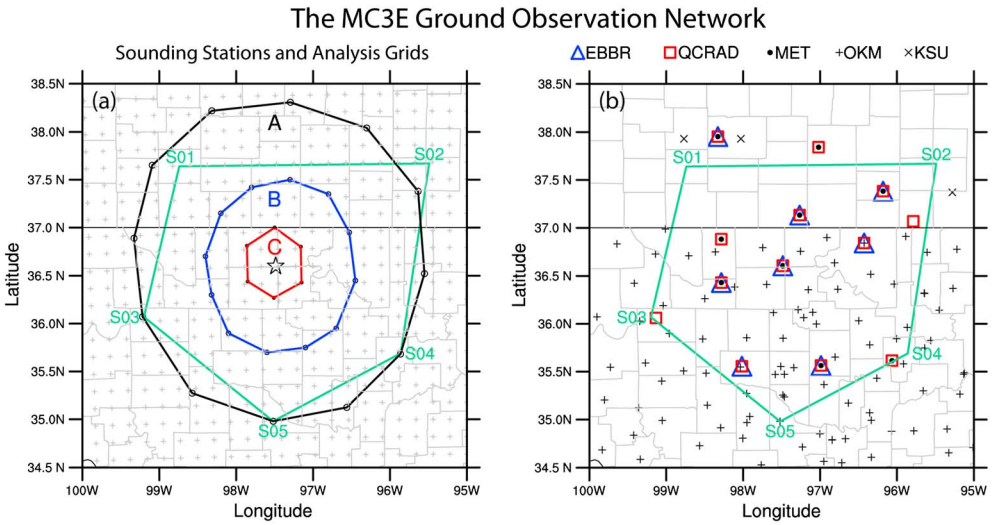

Figure 1. The ground observation network established during MC3E. (a) Sounding stations (S01–S05 and central facility), variational analysis grid points (dotted), and ARM SGP CF (star). Black circle denotes variational analysis domain A with a diameter of 300 km centered at SGP CF; blue circle denotes domain B with a diameter of 150 km; red circle denotes domain C with a diameter of 75 km. (b) Other surface stations available at the ARM SGP site.

possible amount to conserve column-integrated mass, moisture, and static energy so that the final analysis data set is dynamically and thermodynamically consistent. The required observational constraints include the surface and TOA radiative fluxes, surface latent and sensible heat fluxes, and surface precipitation. This method has been successfully used to process data collected in major ARM field campaigns at its permanent research sites, such as the Oklahoma SGP site [*Zhang et al*., 2001], the North Slope of Alaska site [*Xie et al*., 2006], and the Tropical Western Pacific-Darwin site [*Xie et al*., 2010a]. It was also used for analyzing data from the Tropical Rainfall Measuring Mission (TRMM) Kwajalein Experiment, the TRMM Large-Scale Biosphere-Atmosphere Experiment, and the TRMM South China Sea Monsoon Experiment [*Schumacher et al*., 2007]. In this section, we provide some technical details about the objective analysis of the MC3E observations.

The MC3E sounding array consists of five sounding stations centered on a sixth site at the ARM SGP central facility (CF) (Figure 1a). The sounding array covers an area with a diameter of approximately 300 km. The variational analysis technique described above was applied to MC3E over a domain that contains the five boundary sounding stations S01–S05 (Domain "A" in Figure 1a). This is the ARM standard analysis domain that was used to produce the forcing data for earlier ARM field campaigns at SGP. To examine how the analyzed budget structure changes with the analysis domain size, we also perform additional analyses over two smaller domains (Domains "B" and "C" in Figure 1a), which represent an area

Table 1. Required Constraint Variables in the Variational Analysis and Their Data Sources

Constraint Variables	Data Sources
Surface latent and sensible heat fluxes	Best-Estimate Fluxes from Energy Balance Bowen Ratio Measurements and Bulk Aerodynamics Calculations
Surface radiative fluxes	Data Quality Assessment for ARM Radiation Data
Surface precipitation	Arkansas-Red Basin River Forecast Center (ABRFC) 4 km rain gauge adjusted WSR-88D radar measurements and the bias-corrected National Severe Storm Laboratory (NSSL) National Mosaic and Multisensor Quantitative Precipitation Estimate (QPE) (NMQ) Next-Generation Radar (NEXRAD)-based precipitation
Surface meteorology	Surface Meteorological Instrumentation Oklahoma Mesonet Kansas State University Mesonet
TOA radiative fluxes	GOES satellite retrieved SW/LW fluxes

Table 2. Upper and Lower Bounds of the Precipitation Uncertainty Range[a]

Cases	Upper Bound	Lower Bound
$(P_a \times P_n) \neq 0$	$\text{Max}(P_a, P_n) \times (1 + 0.4)$	$\text{Min}(P_a, P_n) \times (1–0.4)$
$(P_a \times P_n) = 0$	$\text{Max}(P_a, P_n) \times (1 + 0.4)$	0

[a] P_a is the domain mean precipitation rate based on ABRFC, while P_n is the domain mean value from NEXRAD NMQ data.

with diameters of approximately 150 km and 75 km, respectively. The large-scale forcing derived over these domains with different sizes could be used for modeling various-scale convective systems. Locations of the sounding stations and the analysis grid points are shown in Figure 1a. It is seen that the location of these sounding stations either overlaps with the analysis grid or is close to it. In the following discussion, the analysis domain refers to the standard domain A unless the two smaller domains are explicitly indicated. The temporal and vertical resolutions used in all analyses are 3 h and 25 hPa, respectively.

All sounding sites used Vaisala model RS92-SGP radiosondes. Humidity measurements from these radiosondes include several well-documented errors including bias (systematic) errors, random errors, and sensor time-lag errors [e.g., *Milosevich et al*., 2009]. We have applied the empirical mean bias correction derived by *Milosevich et al*. [2009] through an intercomparison study with a cryogenic frost-point hygrometer. After applying these corrections a comparison with independent observations of the precipitable water vapor from a microwave radiometer at the ARM SGP CF showed reasonable agreement and gave confidence that the corrections were correct. More details regarding the MC3E sounding operations, data processing, and analysis can be found in *Jensen et al*. [2014].

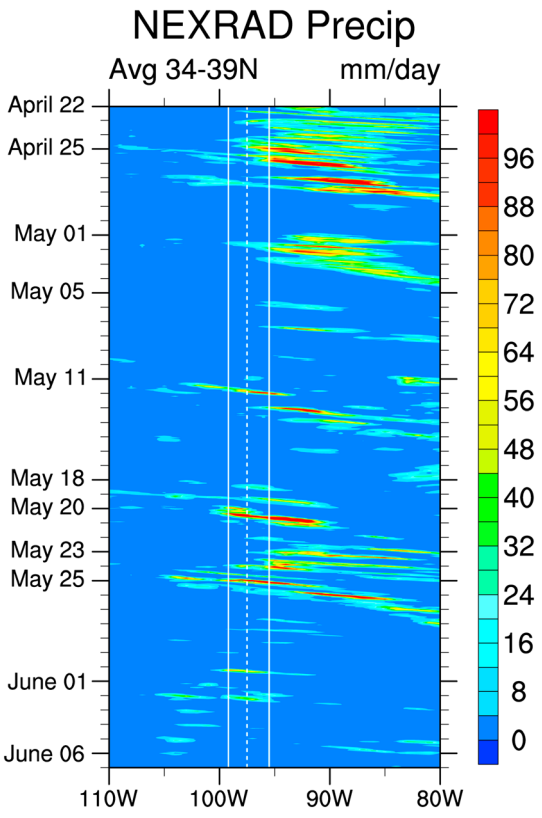

Figure 2. Hovmöller diagram of hourly bias-corrected NOAA NMQ-NEXRAD precipitation averaged over 34°N to 39°N. The east-west boundary of the sounding array is bounded by the two solid white lines, and the dashed white line indicates the location of the ARM SGP CF.

The dry bias-corrected radiosondes described in *Jensen et al*. [2014] are used in the analysis. The objective analyses of the sounding measurements of temperature, wind, and humidity at the analysis grid points are done with the background fields from the National Oceanic and Atmospheric Administration (NOAA) rapid update cycle (RUC) analyses using the Cressman scheme [*Cressman*, 1959]. The *Cressman* scheme uses a weighting function that depends on the distance between an observation station and an analysis grid point, as well as the difference between observations and the background. The interpolation is carried out for the difference field between observations and the background. If there is no measurement within a specified distance of an analysis grid point, the scheme will only take the background field as the analysis.

The required surface and TOA constraints for the variational analysis are obtained from the ARM SGP extensive surface observation network and the Geostationary Operational Environment Satellite (GOES) narrowband brightness temperature, respectively. Table 1 lists these required constraint variables and their data sources. Locations of these surface instruments are shown in Figure 1b. Sampling of surface measurements in calculating area-averaged quantities is a potential concern for

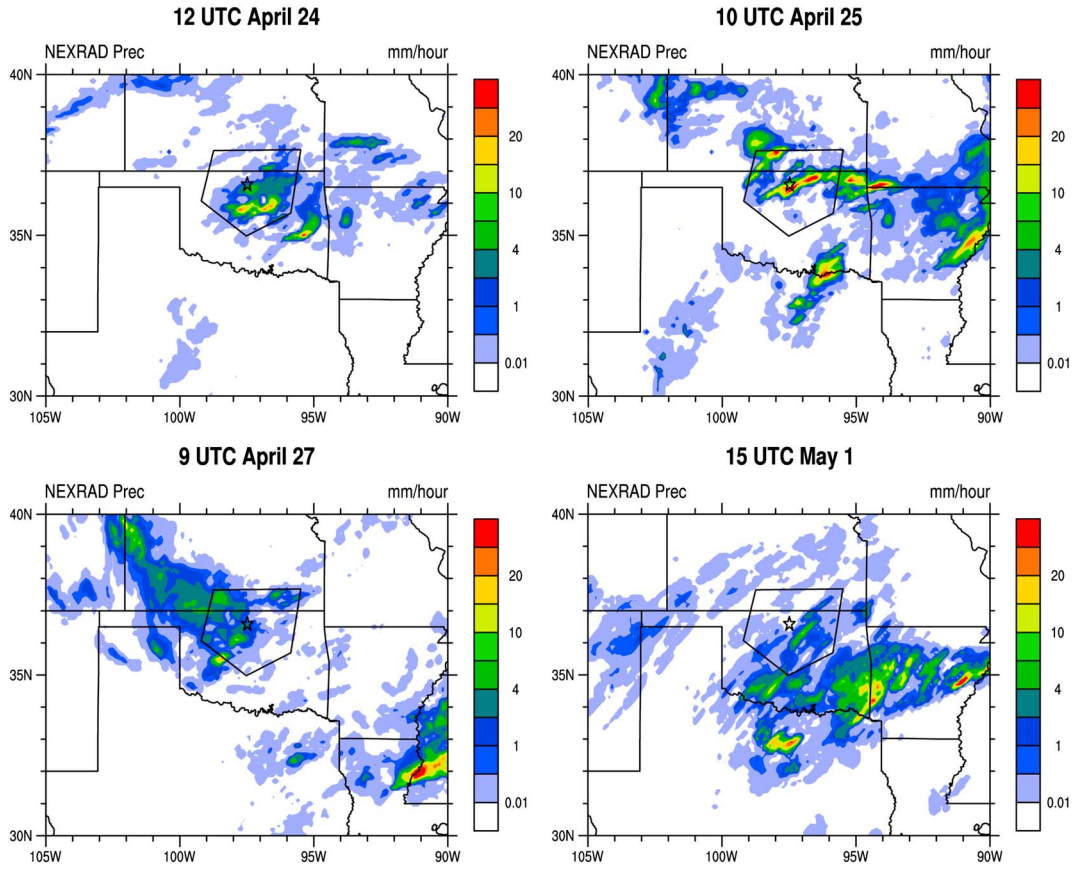

Figure 3. Images of the NOAA NMQ-NEXRAD precipitation for four selected precipitation events associated nocturnal elevated convection. The pentagon in these figures denotes the MC3E sounding domain. Local time in SGP is 5 h less than universal time (UTC).

variables that have large spatial variabilities. To reduce sampling biases, we lay the 0.5° × 0.5° GOES grids over the analysis domains and then derive the surface quantities in each small grid box. If there are actual measurements within a 0.5° × 0.5° grid box, simple arithmetic averaging is used to obtain the subgrid means. If there is no actual measurement in a 0.5° × 0.5° box, then a Barnes scheme [*Barnes*, 1964] is used to fill the missing data. Domain averages of these quantities are obtained by using values from the 0.5° × 0.5° grid boxes within the respective analysis domains. More details of the variational analysis method and its implementation to ARM data can be found in *Zhang et al*. [2001].

Earlier studies [*Zhang et al*., 2001; *Xie et al*., 2004a] have shown that surface precipitation is the most dominant constraint for the variational analysis during precipitation periods. To investigate the impact of uncertainties in the surface precipitation on the derived budget terms, an ensemble analysis, which contains 13 ensemble members, was carried out using the constrained variational objective analysis approach. The uncertainty range in precipitation is derived based on differences in two independently developed precipitation data sets: the Arkansas River Basin Forecast Center (ABRFC) precipitation [e.g., *Young et al*., 2000] products and the bias-corrected National Severe Storm Laboratory (NSSL) National Mosaic and Multisensor Quantitative Precipitation Estimate (QPE) (NMQ) Next-Generation Radar (NEXRAD)-based precipitation [e.g., *Zhang et al*., 2005] products (Table 1). The uncertainty range also takes into account that the fractional root-mean-square error (RMSE) of areal estimates of rain is often found to exceed 40% (relative to mean rain rate) in conventional radar-based rainfall algorithms [e.g., *Ryzhkov et al*., 2005; *Giangrande et al*., 2014]. We assume maximum spatial and temporal correlation of precipitation rate uncertainties across the

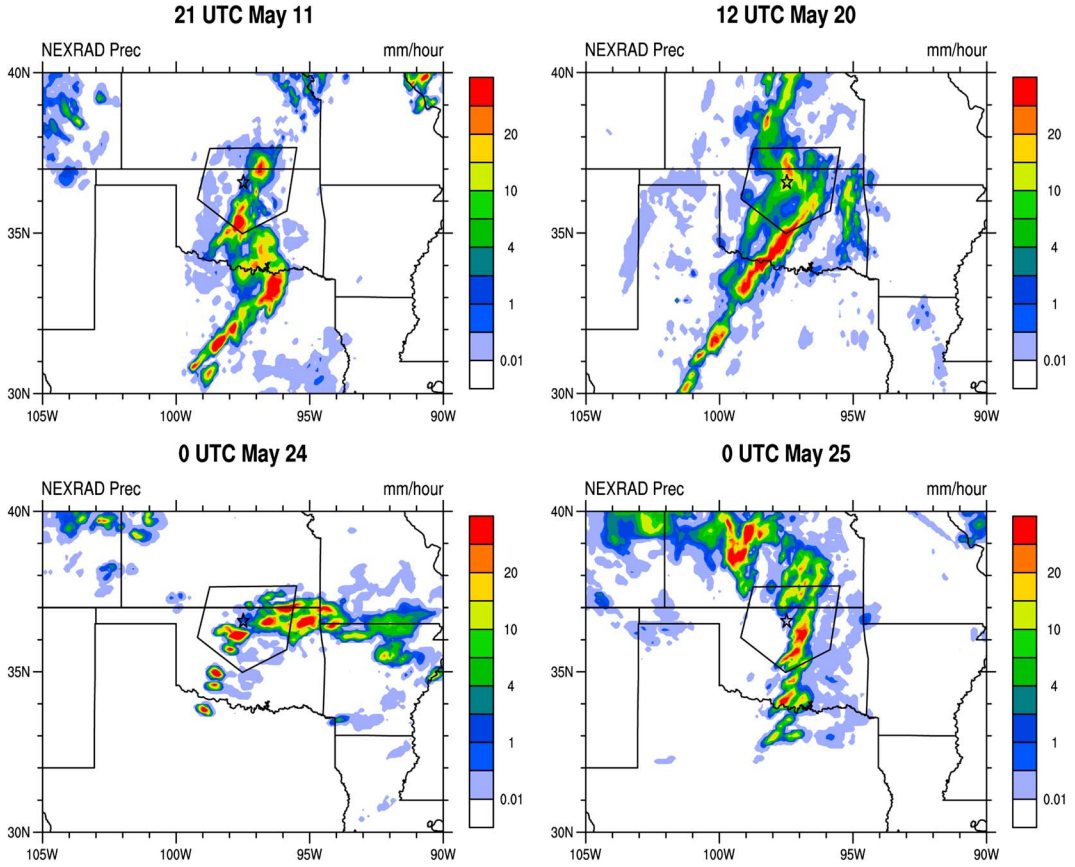

Figure 4. Images of the NOAA NMQ-NEXRAD precipitation for four selected precipitation events associated with organized convection. The pentagon in these figures denotes the MC3E sounding domain. Local time in SGP is 5 h less than universal time (UTC).

analysis domain. The upper and lower bounds of the precipitation uncertainty range are listed in Table 2. The first 11 ensemble members of precipitation rates are calculated by

$$P_i = P_L + (P_U - P_L) \times i \times 0.1 \quad (1)$$

where i =0 to 10. Two additional ensemble members are the precipitation rates obtained from ABRFC product and NSSL NMQ product, respectively. Note that the ensemble analysis is only performed over Domain A.

3. Overview of the Observed Convective Systems and Their Environments

The Hovmoller diagram of hourly NMQ-NEXRAD precipitation (Figure 2) depicts the time evolution and east-west propagation of the convective systems that passed over the ARM SGP site. Note that the west-east boundary of the sounding array is bounded by the two solid white lines in the figure. Late April and early May during MC3E featured discrete convective storms, most often characterized as elevated nocturnal events having associated widespread stratiform precipitation. After an extended dry period, the events during the middle to late May were well-organized convection (squall line) and severe supercell thunderstorm events typically initiating to the west of the main ARM site and propagating over the site.

The earliest storms developed across northern parts of Oklahoma and along an elevated front, aided by middle to upper level ascent associated with the passage of an upper level trough. These nighttime elevated convective cells were relatively shallow in depth, removed from the surface boundary forcing features located in southern Oklahoma also responsible for ongoing convection. Corresponding radiosondes showed a very dry and stable boundary layer, as well as elevated instability in midlevels above 600 hPa. In contrast, the organized convective events from middle to late May were mostly associated with substantial larger-scale forcing including the passage of strong surface features (cold front, dry line), as well as additional afternoon cell triggering supported by the passage of shortwave troughs. For simplicity, we use the labels "Elevated

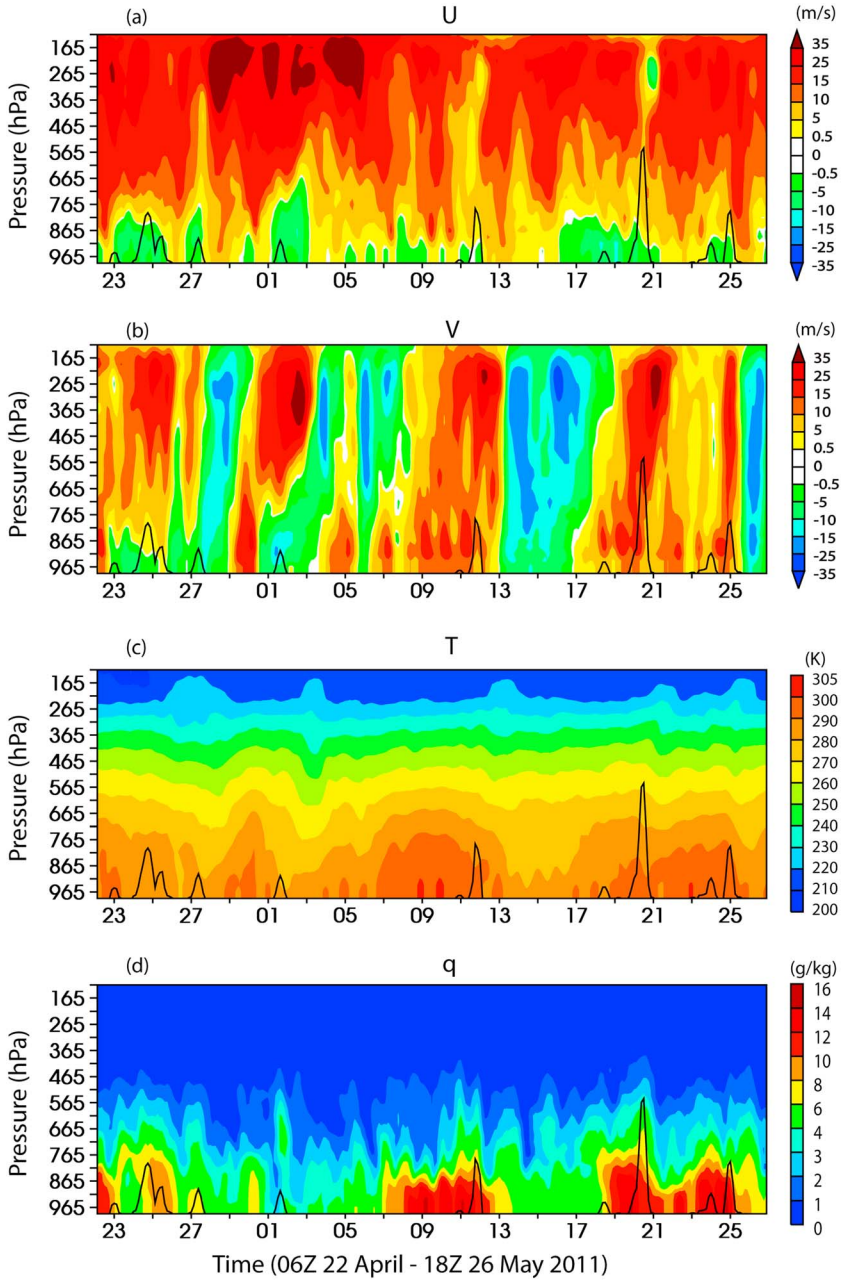

Figure 5. The time-pressure cross sections of the analyzed (a) zonal wind (U [m s^{-1}]), (b) meridional wind (V [m s^{-1}]), (c) temperature (T [K]), and (d) water vapor mixing ratio (q[g kg^{-1}]) over the analysis domain during MC3E. In these figures, black lines are surface precipitation rates. A three-point running mean was applied to these fields for display purposes.

Convection" to refer to the late April and early May discrete nocturnal elevated convective episodes and "Organized Convection" to refer to the middle to late May squall line and severe supercell thunderstorm events in discussions that follow.

The above discussion indicates that the convective events observed during MC3E were often associated with mesoscale propagating convective systems which may not be well captured by the current sounding array with a size of around 300 km by 300 km. However, by examining the NMQ-NEXRAD precipitation data over the region (not shown), we found that almost all of individual convective cells related to the convective events considered for this study initiated well within (23 and 24 April and 1, 11, 24, and 25 May) and/or typically toward the western edge of the sounding array (25 and 27 April and 20 May). These systems then continued to grow and enhance within the sounding array forced by the large-scale disturbance in the

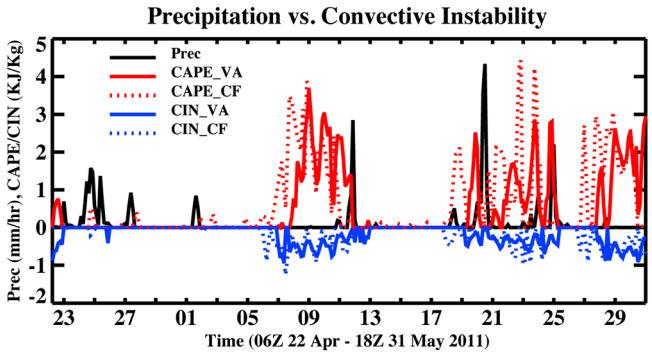

Figure 6. Observed the domain-averaged ABRFC surface precipitation rates (mm hr^{-1}) and CAPE/CIN (KJ/Kg) computed from domain-averaged soundings (CAPE-VA/CIN_VA) and CF soundings (CAPE_CF/CIN_CF).

domain. Figures 3 and 4 show snapshots for four selected Elevated Convection and four Organized Convection, respectively, during their mature stages based on NMQ-NEXRAD instantaneous radar precipitation rates. These selected convective events will be discussed in more detail in the following sections. These figures clearly show that a large portion of each storm was located within the sounding array, which indicates that the large-scale structures and diabatic heating and moistening and their interactions could be reasonably captured by the sounding array. It is seen that the squall line (11 and 20 May) and deeper supercell (24 and 25 May) convective episodes exhibit a much higher intensity than the early season elevated convective storms.

The large-scale circulation during MC3E was characterized by strong westerlies in the middle to upper troposphere where a southerly wind and a northerly wind generally alternated between wet and dry periods (Figures 5a, 5b, and 5d). In the lower troposphere, north easterlies prevailed during the periods when the elevated storms happened while southeasterlies dominated the squall line and deeper convective periods. The southeast winds brought in a sufficient warm moist air to the experiment region from the Gulf of Mexico to support the squall line systems (not shown). As shown in Figures 5c and 5d, the low-level atmosphere (below 715 hPa) was warmer and wetter for squall lines compared to the earlier scattered elevated storms. The low-level warming and moistening provided a favorable large-scale condition to initiate and maintain these intense convective events.

Figure 6 shows the time series of domain mean precipitation rates from ABRFC product and the convective available potential energy (CAPE) and convection inhibition (CIN) calculated from the domain-averaged soundings and CF soundings, respectively. CAPE is calculated under the assumption that an air parcel ascends along a reversible moist adiabat with the originating level at the surface. CIN is the negative value of CAPE between the level of free convection and the surface. For the CAPE/CIN at the CF ARM radiosonde observations are used.

The late April and early May elevated convective storms occurred in a rather stable environment, in which CAPE was weak or no CAPE was detected particularly by the domain mean soundings. This is largely due to the fact that these systems occurred at night (see Table 3) with a very stable boundary layer. It is also noticed that the boundary layer was very dry during these periods. As shown in Figure 7a, which displays the initial soundings at the CF for the 1 May event, the air was very dry at levels below 600 hPa while it was close to saturation at levels between 600 hPa and 500 hPa. This would suggest that convection might initiate at midlevels for this event. In addition to synoptic forcings such as the middle to upper level ascent associated with the passage of an upper level trough as discussed earlier, the midlevel convection might be also partially due to a destabilization process caused by the middle and upper level clouds that were observed just before these scattered storms occurred as shown later. Presumably, the cooling at

Table 3. Classification of Time Periods for the Selected Scatter Storms and Squall Lines[a]

Stage	Scatter Storms Observation times	Squall Lines Observation times
1	00Z 24 Apr, 00Z 27 Apr, 06Z 1 May	12Z 11 May, 18Z 19 May, 18Z 23 May, 15Z 24 May
2	09Z 24 Apr, 06Z 25 Apr, 03Z 27 Apr, 09Z 1 May	15Z 11 May, 06Z 20 May, 21Z 23 May, 18Z 24 May
3	12Z 24 Apr, 09Z 25 Apr, 06Z 27 Apr, 09Z 27 Apr, 12Z 1 May, 15Z 1 May	18Z 11 May, 21Z 11 May, 12Z 20 May, 00Z 24 May, 21Z 24 May, 00Z 25 May
4	15Z 24 Apr, 12Z 25 Apr, 12Z 27 Apr, 18Z 1 May	00Z 12 May, 18Z 20 May, 03Z 24 May, 03Z 25 May

[a]Local time in SGP is 5 h less than universal time (Z).

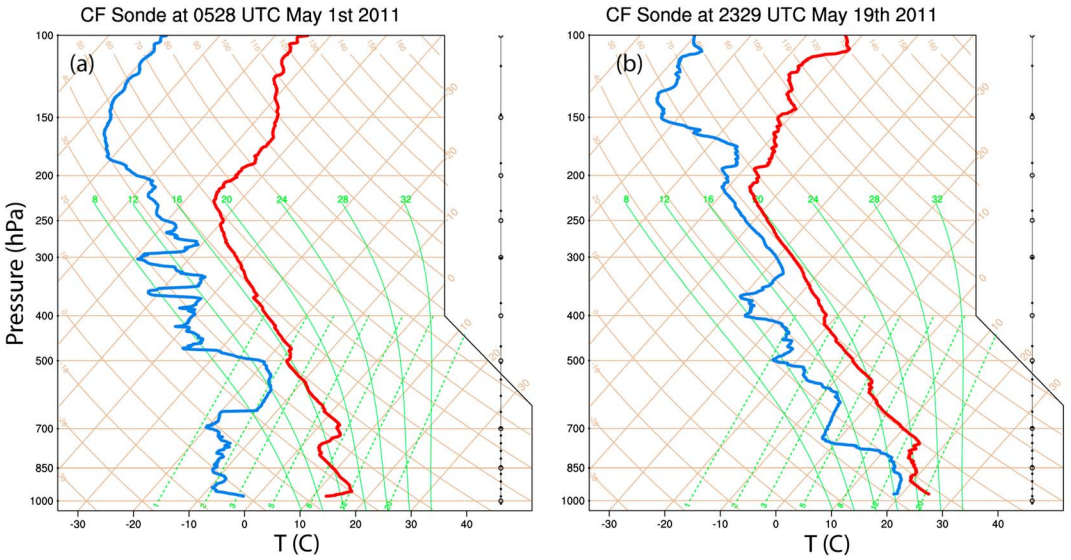

Figure 7. Temperature (*T*) and dew point soundings (Td) at the time right before convection occurred for (a) the 1 May case and (b) the 20 May case.

cloud top and warming at cloud base by longwave radiation destabilized the atmospheric column below a high stratiform layer and initiated convection at midlevels. The depth of the unstable layer increased as the systems continued to evolve. This eventually led to deep convection that developed from the boundary layer. This upper level destabilization process through cloud-radiation interactions was suggested by *Lee et al.* [2010] to be one of the major mechanisms for the formation of nocturnal deep convection at SGP through a cloud-resolving modeling study. We have further examined the dynamic CAPE change rates as defined in *Xie and Zhang* [2000] to see if large-scale upward motion and low-level moisture convergence could act to destabilize the atmosphere. We found that there is no surface-based CAPE detected due to the large-scale forcing. This further implies that the elevated convection is likely caused by top-down destabilization through cloud-radiation interaction and/or middle-upper level disturbances.

In contrast, the middle and late May convective regimes occurred in the morning or early afternoon (Table 3). Large CAPE with strong diurnal variation was diagnosed before the thunderstorms developed. CIN is just opposite to CAPE, acting to prevent convection from consuming the CAPE immediately when it is generated. The initial soundings at the CF were much warmer and moister in the lower troposphere compared to the elevated storm soundings. An example is shown in Figure 7b for a strong squall line that was observed on 20 May. It is seen that the soundings were near saturation at levels below 800 hPa, while they were rather dry in the middle troposphere, suggesting that convection had its roots in the destabilized boundary layer.

The large diurnal variability exhibited in CAPE is due to the strong solar diurnal heating over land in warmer months. It is clear that a positive CAPE is not a sufficient condition to trigger convection. This presents a big challenge for the CAPE-based closure schemes implemented in many climate models for deep convection. Earlier studies have shown that most climate models fail to capture the nocturnal convection and produce overly active convection during the day in the warm season at SGP [*Xie and Zhang*, 2000; *Xie et al.*, 2004b].

Figure 8a shows the clouds measured by the ARM surface remote sensing instruments, including a 35 GHz Ka-band ARM Zenith-pointing Radar, Micropulse Lidar (MPL), and laser ceilometers at the ARM SGP CF. The figure is constructed by integrating measurements from KAZR, MPL, and laser ceilometers using the ARSCL (Active Remote Sensing of CLouds) algorithm [*Clothiaux et al.*, 2000; *Kollias et al.*, 2007] with the method described in *Xie et al.* [2010b], which removes the radar echoes below the ARSCL cloud base using the ARM laser ceilometers and micropulse lidar measurements. The observed clouds correspond well to the relative humidity (RH) field (Figure 8b), which shows a very dry midtroposphere during nonprecipitating

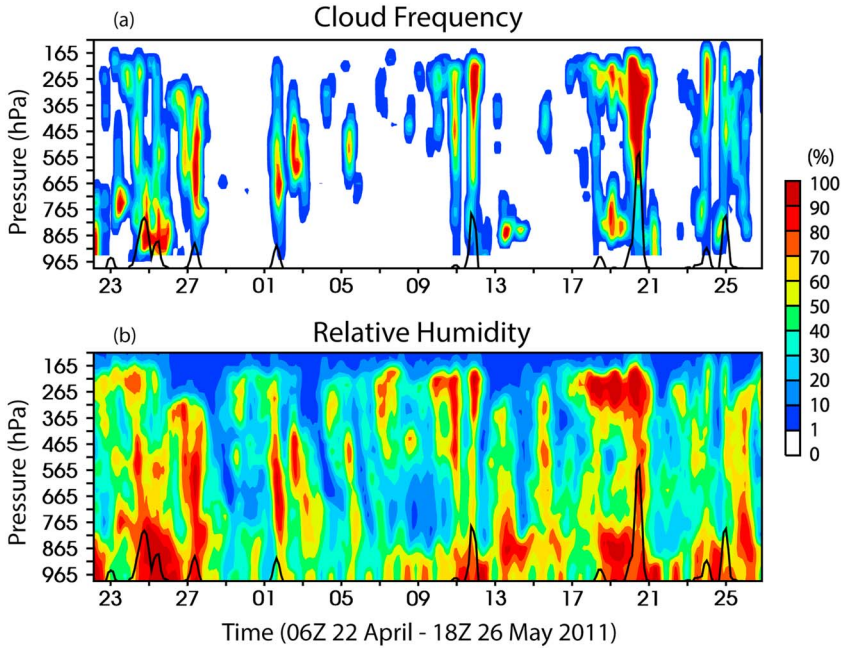

Figure 8. The time-pressure cross sections of (a) cloud frequency of occurrence (%) at CF and (b) the analyzed relative humidity (with respect to ice for $T < 00°C$) (%) over the analysis domain during MC3E. In these figures, black lines are surface precipitation rates. A three-point running mean was applied to these fields for display purposes.

periods. The dry air is mainly a result from subsidence and horizontal advection that transported drier air into the experiment region, which will be discussed later.

There are distinct features in the clouds and RH between the earlier elevated convective storms and the later squall line and supercell events as shown in the composite profiles (Figure 9). The composite analysis is conducted to better understand how large-scale flow affects atmospheric stability and interacts with convection. Since both types of convective systems observed during MC3E are primarily associated with propagating convective episodes and have a short lifetime, it is difficult to perform a typical life cycle analysis. The composite analysis is done here by classifying the progression of these systems into four stages based on the intensity of diabatic heating. Stage 1 is the time right before these convective systems initiate where the diabatic heating is usually less than 1 K/day. Stage 2 is the period when convection grows but the heating is often 40% less than at Stage 3. Stage 3 is the time when the systems are well developed within the analysis domain. This is often the time when precipitation or diabatic heating reaches their maximum values. Stage 4 is a time when the heating has decreased substantially, usually 40% less than at Stage 3. All of the eight major MC3E convective events shown in Figures 3 and 4 are utilized to construct these composite profiles. Since the 25 April case occurred right after the 23 and 24 April event, no Stage 1 is identified for it. The observation times for the selected cases at each stage are listed in Table 3.

Before the elevated systems developed, clouds associated with the trailing stratiform region of other convective systems that have already propagated to the east of the site were located primarily in the upper troposphere, having a general absence of clouds below 765 hPa (Figure 9a). This is consistent with the very dry boundary layer where RH is less than 50% (Figure 9c). The longwave cooling at cloud top and warming from below is likely one of the major mechanisms responsible for the initial destabilization of the atmospheric column at midlevels. As these storms continued to evolve, clouds began to occur at low-level and midlevel associated with a large increase of RH there. The increase RH is mostly due to positive advection of moisture (probably along with cloud) into the array as shown later. The top-down destabilization process was discussed extensively in *Lee et al.* [2010] and was also found in other modeling and observational studies [e.g., *Webster and Stephens*, 1980; *Randall et al.*, 1991]. Despite the weak peak seen around 265 hPa, the majority of clouds were still located at middle and low levels at Stages 3 and 4 when the storms were at their maximum intensity or late development stage.

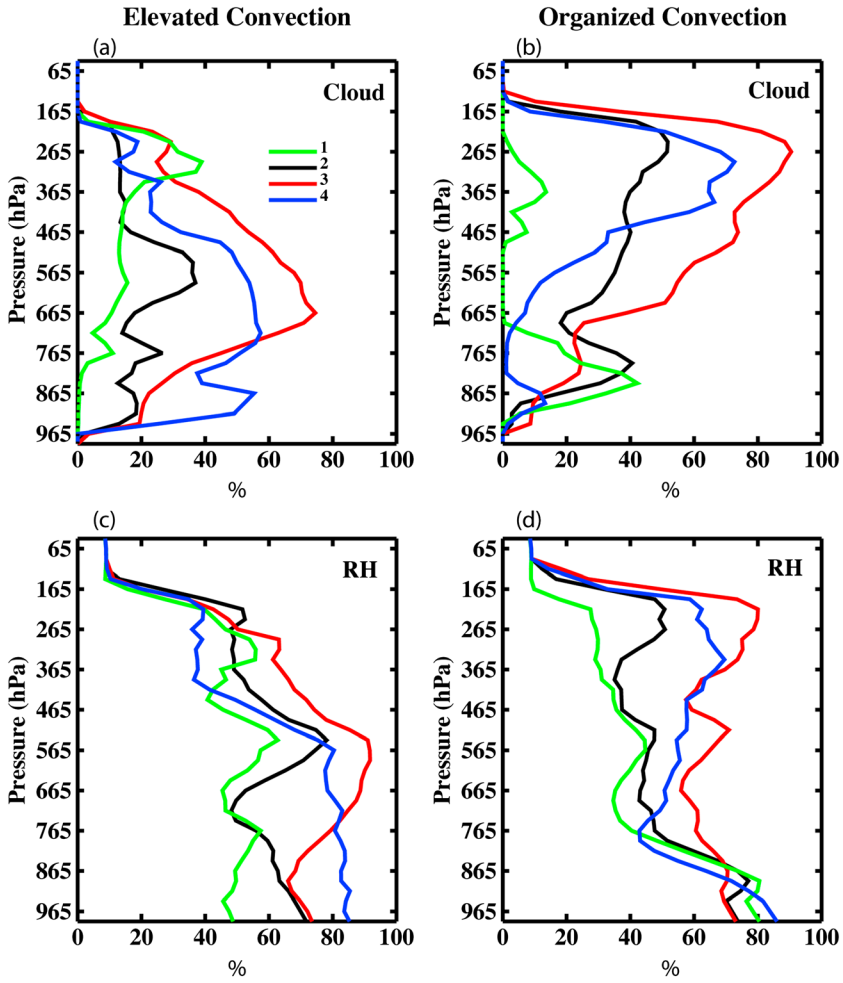

Figure 9. Composite profiles of (a and b) cloud frequency of occurrence and (c and d) relative humidity at different stages of convective systems. Elevated convection (Figures 9a and 9c); Organized convection (Figures 9b and 9d). The periods included in the average and the stages 1–4 are listed in Table 3.

Compared to the elevated storms, the organized convective events occurred in an environment with a very moist boundary layer and a plenty of low clouds (Figures 9b and 9d). However, the middle and upper troposphere were very dry and had few clouds during Stage 1. This is different from tropical systems that often show a significant amount of middle level clouds acting to moisten midtroposphere preceding the major convective systems [*Johnson et al.*, 1999]. The lack of congestus stage may be partially due to the combination of small number of cases and a vertical point measurement, which may miss the developing stage of the storm. However, as discussed later radiosonde data indicate a divergence layer between 665 hPa and 365 hPa, consistent with the lack of midlevel clouds. This suggests that more cases and scanning cloud radars are needed to fully characterize various stages of the convections. In contrast again with the nocturnal elevated storms, the middle and particularly high clouds developed rapidly as the systems continued to evolve. The peak was seen around 265 hPa when the systems were at their maximum intensity, suggesting the formation of deep convection with large anvils in these intense squall lines at this stage.

Corresponding to these convective activities, the analyzed large-scale circulation featured low-level convergence and upward motion. The maximum ascending motions were seen in the middle and upper troposphere (Figures 10). Strong low and midlevel divergence and downward motion dominated the dry periods. The composite profiles (Figure 11) clearly demonstrate the structure difference in the large-scale

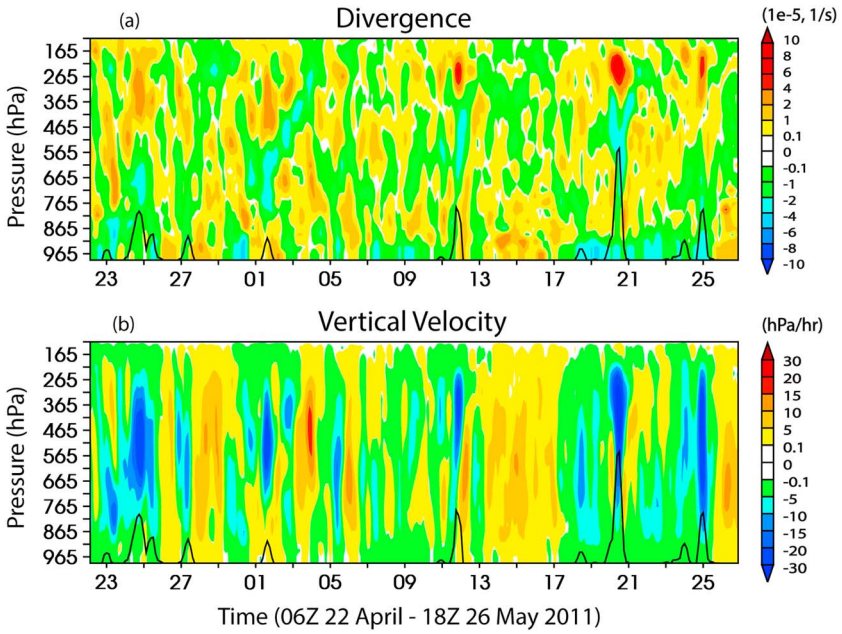

Figure 10. The time-pressure cross sections of the analyzed (a) divergence (10–5, s^{-1}) and (b) vertical velocity (hPa h^{-1}) over the analysis domain during MC3E. In these figures, black lines are surface precipitation rates. A three-point running mean was applied to these fields for display purposes.

dynamic fields between the elevated weaker storms and the squall line and supercell cases. For example, the considerable low-level convergence shown in the deeper convective atmosphere (Figure 11b) at Stage 1 is not seen in the elevated discrete storms (Figure 11a). The mean divergence profile in the squall lines shows divergence between 665 hPa and 365 hPa, consistent with the general lack of clouds at these levels. At Stage 3 when convection reaches its maximum intensity, all convective events exhibit strong convergences that extend from the surface to the middle troposphere. The nondivergence level is higher in the squall lines than the elevated storm cases, which leads to a much stronger and deeper ascending motion diagnosed from the squall line soundings (Figures 11c and 11d). The divergence behaviors were consistent with those found in *Hopper and Schumacher* [2009, 2011], which systematically examined variations in divergence profiles associated with environmental and storm type differences (including elevated convection and organized convection) in midlatitude convective systems observed in Southeastern Texas. The level of the largest upward motion is located at around 515 hPa in the elevated storms, while it is around 365 hPa in the squall lines and deeper convective cases. These mature stage behaviors were consistent with observed profiles of the vertical velocity available from ARM 915 MHz profilers during MC3E campaign events [e.g., *Giangrande et al.*, 2013]. The vertical structure of upward motion in the squall lines and deeper convective cases is also similar to that shown in *Gallus and Johnson* [1991] that studied an intense midlatitude squall line case observed during the OK PRE-STORM (Oklahoma-Kansas Preliminary Regional Experiment for STORM-Central) project, but the level of maximum upward motion is slightly lower (400 hPa) in *Gallus and Johnson* [1991] At Stage 4, the later May events show a double-peak structure in the upward motion with the primary peak located around 365 hPa and the secondary, much weaker one at 865 hPa, associated with stratiform clouds and shallow convection. This feature is not clearly seen in the earlier MC3E storms.

It should be noted that the ARM cloud information is not assimilated into the variational analysis. The consistency between clouds and the analyzed large-scale structures provides an additional check on the quality of the heat and moisture budgets diagnosed from the variational analysis. These results suggest that the variational analysis has produced a reasonable dynamic structure of these cloud systems based on the MC3E soundings, which gives us confidence in the following budget analysis.

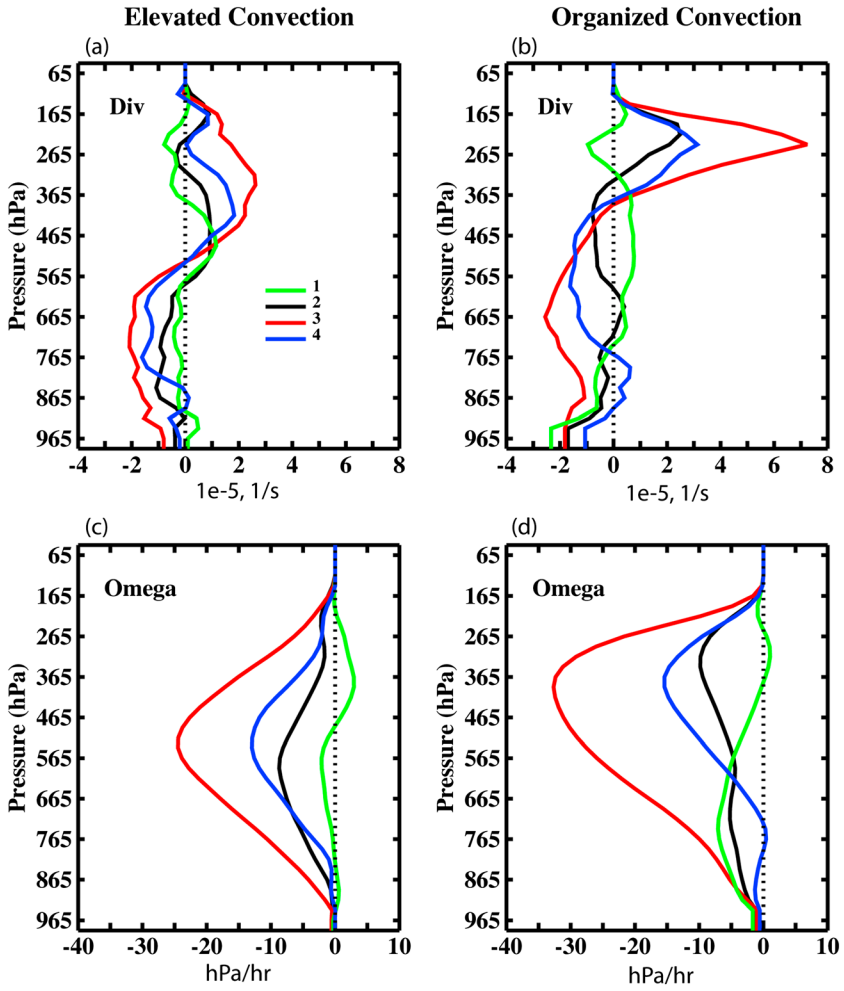

Figure 11. Composite profiles of (a and b) divergence and (c and d) vertical velocity at different stages of convective systems. Elevated convection (Figures 11a and 11c); Organized convection (Figures 11b and 11d). The periods included in the average and the stages 1–4 are listed in Table 3.

4. Heat and Moisture Budgets

As defined in *Yanai et al*. [1973], the heat (Q_1) and moisture budget (Q_2) equations can be written as:

$$Q_1 = \frac{\partial s}{\partial t} + \vec{V}_h \cdot \nabla s + \omega \frac{\partial s}{\partial p} \tag{2}$$

$$Q_2 = -L\left(\frac{\partial q}{\partial t} + \vec{V}_h \cdot \nabla_p q + \omega \frac{\partial q}{\partial p}\right) \tag{3}$$

where s is the dry static energy, q the water vapor mixing ratio, $\vec{v}_h$ the horizontal wind vector, ω the vertical velocity in pressure coordinates, and L the latent heat of vaporization. As discussed earlier, the terms Q_1 and Q_2 are the residuals of heat and moisture budgets and include the collective effects of subgrid-scale processes, such as radiation, convection, and turbulence. In a highly convective situation, heating and drying from convection may have the most significant contributions to Q_1 and Q_2.

4.1. Heat Budget

Figure 12 displays the heat budget terms over the analysis domain. The strong diurnal heating near the surface in both the heat storage term ($\frac{\partial s}{\partial t}$, Figure 12a) and Q_1 (Figure 12b) is due to the strong solar heating and sensible heat flux over land during the day. The fluctuation of Q_1 corresponds well with the surface

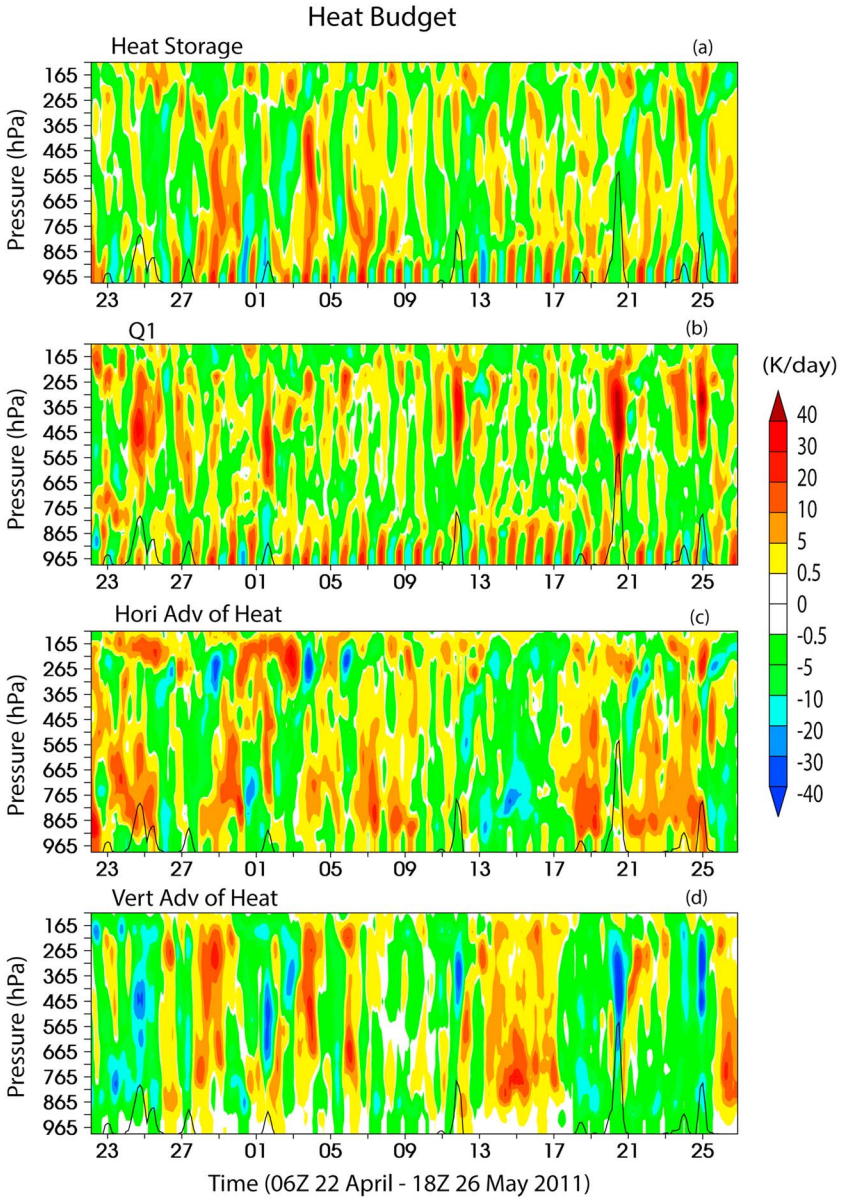

Figure 12. The time-pressure cross sections of the analyzed heat budget terms over the analysis domain during MC3E. (a) Storage term. (b) Diabatic heating rate (Q_1). (c) Horizontal advective tendency of temperature. (d) Vertical advective tendency of temperature. Unit: K d^{-1}. In these figures, black lines are surface precipitation rates. A three-point running mean was applied to these fields for display purposes.

precipitation. Over these periods, a strong heating associated with the latent heat release is diagnosed in the middle and upper troposphere. A cooling is seen in the lower levels, presumably related to the evaporation of precipitation. For most of the experiment period, the horizontal advection of heat ($-\vec{V}_h \cdot \nabla s$, Figure 12c) tends to warm the lower and midtroposphere below 515 hPa and the levels above 265 hPa, and somewhat cool the levels in between. The vertical advection ($-\omega \frac{\partial s}{\partial p}$, Figure 12d) shows a strong middle and upper level cooling over precipitation periods and a strong warming during dry periods. This cooling/warming is primarily associated with the large-scale upward/downward motions as shown in Figure 10b.

More detailed composite analyses of these budget terms are shown in Figures 13 and 14 for the earlier elevated storms and the deeper later events, respectively. For the elevated earlier storms, both Q_1 and the vertical transport of heat (Figures 13b and 13d) are weak due to the lack of convective activities and

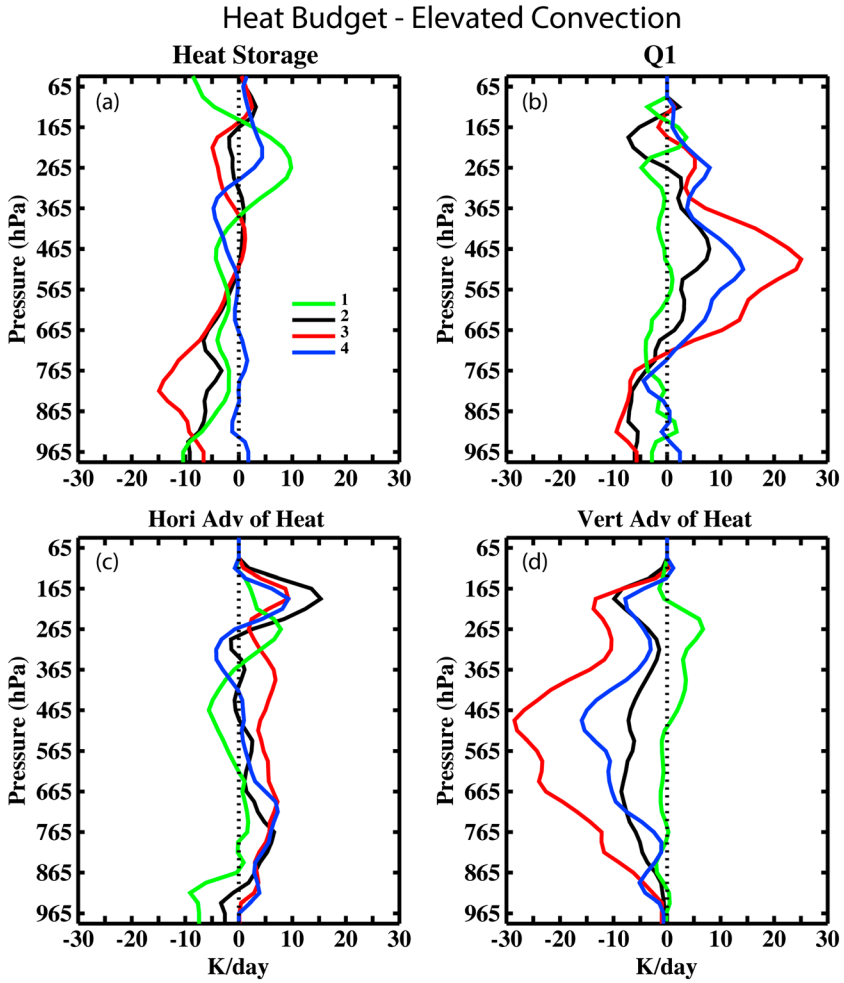

Figure 13. Composite profiles of heat budget terms at different stages (1–4) of elevated convective systems. (a) Storage term, (b) Q_1, (c) horizontal advective tendency of heat, and (d) vertical advective tendency of heat. Units are K d^{-1}. The periods included in the average and the stages 1–4 are listed in Table 3.

upward motions at Stage 1. The horizontal advection of heat (Figure 13c) is the major contributor to the cooling seen near the surface in the storage term (Figure 13a). As the earlier elevated systems start to grow and reach their maturity, the Q_1 profile shows large heating in the middle troposphere and a considerable cooling below, especially at Stages 2 and 3. This structure was also found in earlier studies for midlatitude storms [e.g., *Kuo and Anthes*, 1984]. In tropical convective systems, the heating usually extends through the entire troposphere [e.g., *Xie et al*., 2010a]. The heating in Q_1 at these stages is primarily balanced by the cooling associated with upward motion. The lower level cooling is mainly due to the evaporation of precipitation and clouds.

Q_1 is much stronger and extends much higher in the squall line and supercells when the system reaches its maximum intensity (Figure 14b). Note that the scale in *x* axis used in Figures 14b and 14d is 2 times larger than that in Figures 13b and 13d. The maximum in upper level heating occurs at around 340 hPa for these later May events compared to 515 hPa in the earlier weaker elevated storms when both types of systems reach their maximum intensity. Similar to the elevated events, a notable cooling is also seen in the lower troposphere at Stages 3 and 4. The strong heating in Q_1 is primarily balanced by the cooling from the vertical transport of heat (Figure 14d), leading to a relatively small change in the storage term (Figure 14a). The horizontal advection (Figure 14c) is large in the upper troposphere above 365 hPa and is also important in the lower troposphere. It is worth noting that a cold horizontal advection is seen near the surface before the elevated storms develop, while a near surface warm horizontal advection is found before the deeper and

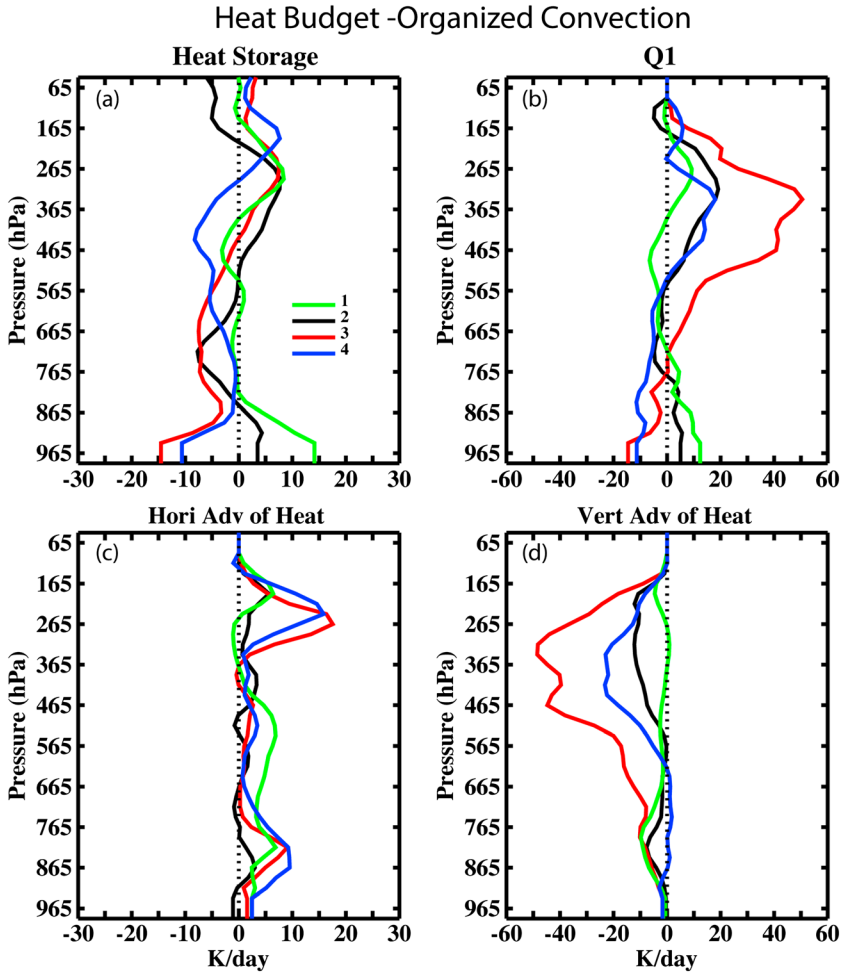

Figure 14. Same as Figure 13 except for organized convection.

squall line systems develop. This reflects the difference in the near surface flow between these two types of convective systems as we discussed earlier. The warming below 815 hPa at Stage 1 in Figure 14b is due to the solar radiation and sensible turbulent flux during the day.

The diagnosed Q_1 profile in the deeper events is similar to that in *Kuo and Anthes* [1984] and *Gallus and Johnson* [1991], which also indicated an upper level heating between 400 hPa and 350 hPa. However, the level of maximum upward motion in *Kuo and Anthes* [1984] is located around 550 hPa, much lower than what found in *Gallus and Johnson* [1991] and the current study. The difference could be partially from the larger domain (550 km × 550 km) used in *Kuo and Anthes* [1984] compared to the 300 km × 300 km domain used in this study. Sensitivity of the analyzed budgets to the analysis domain size will be discussed in section 5. The difference may also suggest variations among different convective systems and the need for more case studies.

4.2. Moisture Budget

The time-pressure cross sections of individual terms in the moisture budget are displayed in Figure 15. In general, the horizontal advection of moisture ($-\vec{V}_h \cdot \nabla_p q$, Figure 15c) plays an important role in moistening the lower troposphere, while the vertical advection ($-\omega \frac{\partial q}{\partial p}$, Figure 15d) is the key process that transports moisture to the middle and upper troposphere for convection to consume. The Q_2 profile (Figure 15b), which is normalized by L, indicates that the drying associated with convection can reach up to 265 hPa in the strong convective events, although the majority of the drying occurs at lower levels. As a result, the storage term ($\frac{\partial q}{\partial t}$, Figure 15a)

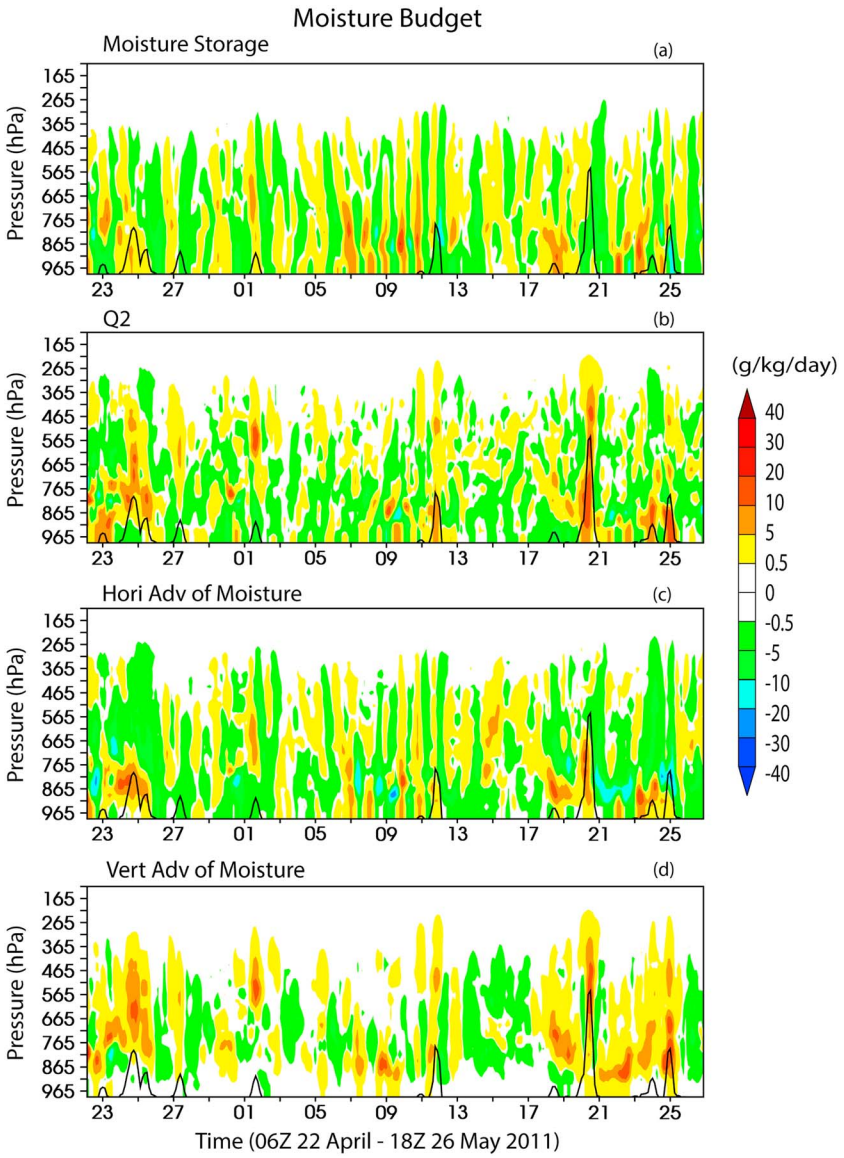

Figure 15. The time-pressure cross sections of the analyzed moisture budget terms over the analysis domain during MC3E. (a) Storage term. (b) Diabatic drying rate (Q_2). (c) Horizontal advective tendency of moisture. (d) Vertical advective tendency of moisture. Unit: g kg^{-1} d^{-1}. In these figures, black lines are surface precipitation rates. A three-point running mean was applied to these fields for display purposes.

generally shows a moistening when the systems are at their early development stages (Stages 1 and 2), and a drying when the systems are well developed or begin to dissipate (Stages 3 and 4), which can be seen clearly in the composite analysis figures (Figures 16 and 17).

For the earlier elevated storms, the storage term shows a weak moistening below 765 hPa (Figure 16a) before the systems develop. This is largely due to the evaporation of clouds and the vertical transport of turbulence fluxes as shown in Q_2 (Figure 16b). The middle and low-level moistening from the horizontal advection (Figure 16c) also contributes to this moistening. At this stage, the vertical advection is weak (Figure 16d). As the systems evolve to Stages 3 and 4, a strong diabatic drying is seen at levels above 865 hPa and a considerable moistening is found below. The middle and upper level diabatic drying is largely offset by the vertical transport of moisture. It is noted that there is a lack of moisture supply from advection near the surface for these storms.

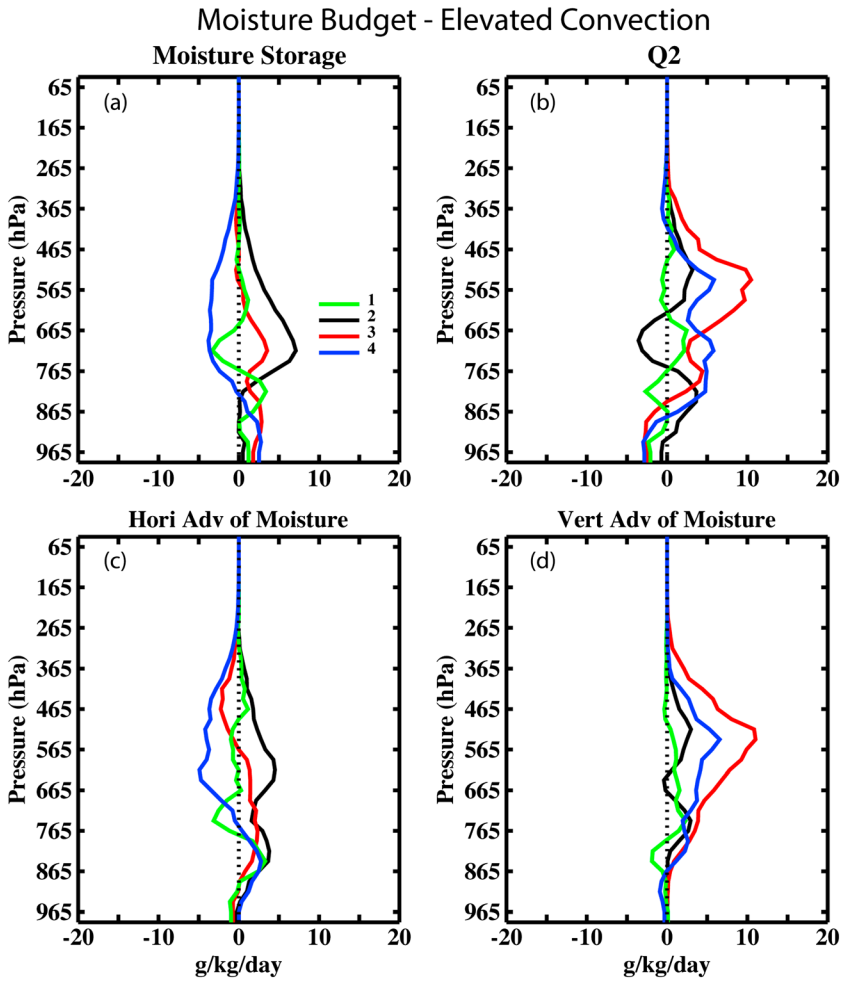

Figure 16. Same as Figure 13 except for moisture budget.

In contrast, there is persistent moisture supply from the horizontal advection near the surface for the later May events (Figure 17c). The low-level moisture supply is from the near-surface southeasterlies, which brings warm moist air into the region. The region of the moist convergence extends up to 565 hPa as the systems grow to Stage 2, which contributes significantly to the moistening at levels above 815 hPa shown in the storage term (Figure 17a). The storage term shows a strong drying at levels below 665 hPa as the systems reach their maxima, primarily due to convection (Figure 17b). The middle and upper moisture supply for convection is purely due to the vertical moisture transport at this stage (Figure 17d). It is noted that the primary peak in Q_2 is located in the lower troposphere along with two weaker peaks located at 715 hPa and 490 hPa, respectively. In addition to the convective drying due to shallow clouds, the vertical turbulent fluxes should also contribute significantly to the low-level drying in Q_2. At Stage 4, Q_2 shows a strong drying at low levels associated with the development of boundary layer clouds and a weak moistening at midlevels due to the evaporation of precipitation. The large drying seen in the storage term at this stage is mainly due to the dry advection of moisture from the horizontal.

The above discussion indicates the important role of the moisture transport in the development of midlatitude convective systems. This is further illustrated in Figure 18, which examines the correlation among the rainfall rates, column-integrated moisture convergence, and moisture storage term for those precipitation events that occurred in April and May. For most of the precipitation events (except for 24 April and 20 May), there is clear evidence that the moisture convergence was leading the convection, acting to moisten the preenvironment for these convective systems. During this period, the moisture storage term showed a considerable increase. It dropped rapidly around the time when the systems reached their maxima. At this stage, consumption

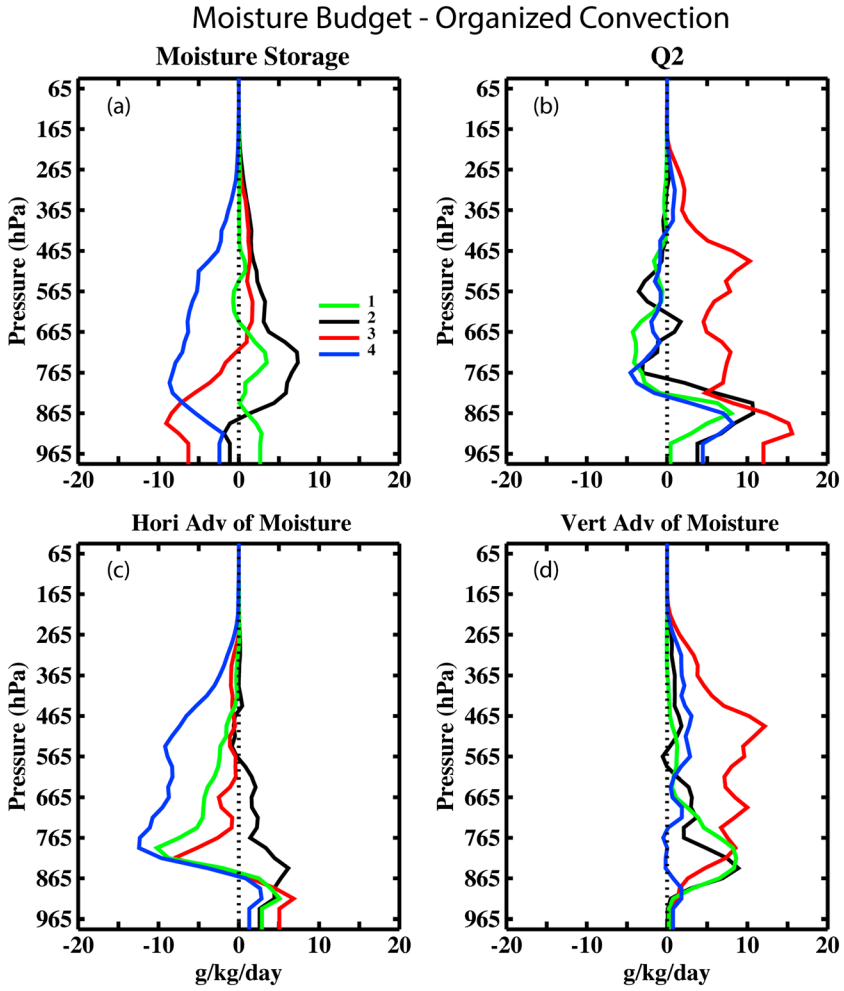

Figure 17. Same as Figure 14 except for moisture budget.

of water vapor by convection (indicated by precipitation) exceeds the large-scale moisture supply, leading to a large decrease of moisture in the integrated storage term.

5. Sensitivity to Precipitation Uncertainty and Domain Size

5.1. Variation of Budget Structure With Precipitation Uncertainty

An ensemble run with 13 ensemble members was performed with the variational analysis over the standard analysis domain A to examine the impact of uncertainties in the surface precipitation on the derived budget structures. The range of uncertainty in the surface precipitation is determined by the difference between the ABRFC product estimate and the NSSL NMQ data set, as well as considering an approximate 40% fractional RMSE for areal estimates of rain associated with radar-based rainfall products. Figure 19a shows the ensemble precipitation rates for the period between 00Z 19 May and 00Z 26 May for demonstration purposes. Similar results are seen for other periods. It is seen that the domain-averaged rainfall rates derived from ABRFC product are very similar to those obtained from the gauge-corrected NMQ product for the 20 May event. Both are close to 50% of the uncertainty range between the upper and lower bound of the estimated precipitation. However, although both products utilize gauge and NOAA WSR-88D NEXRAD radar systems to help produce these estimates, the rainfall rates are significantly larger from the NMQ product for the isolated supercell events that occur on the later campaign days (23–25 May). This spread is to be expected based on the details of how each product handles isolated convective events possibly containing hail and the associated precipitation estimates therein.

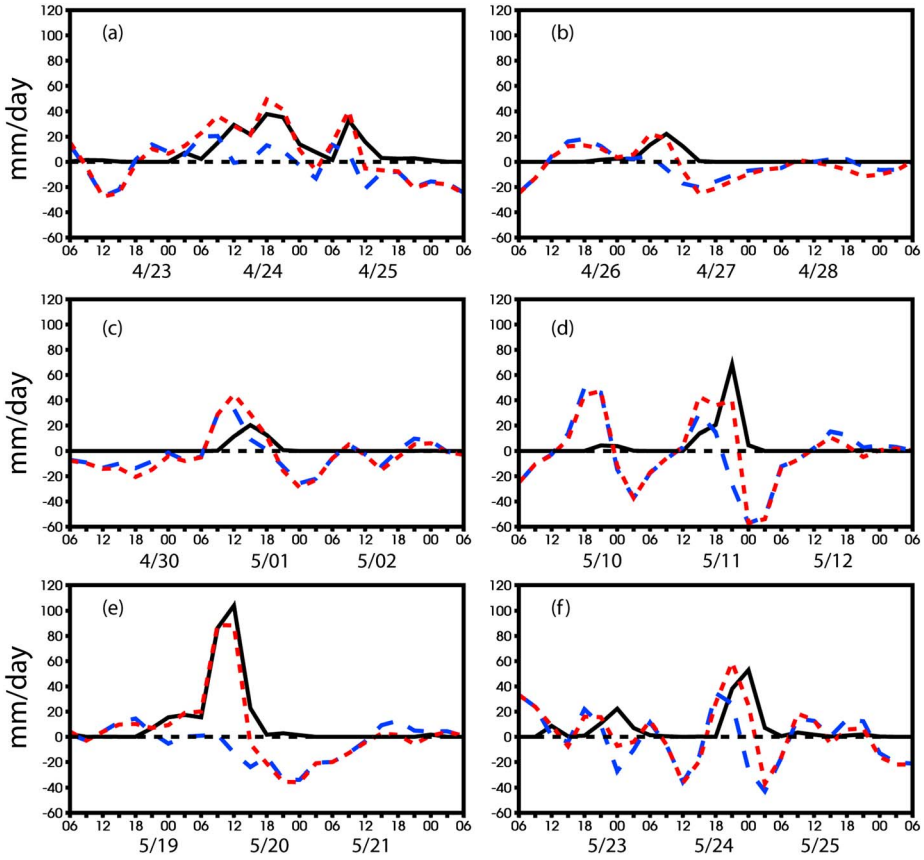

Figure 18. Precipitation rates (solid black lines) and vertically integrated moisture convergence (red dashed lines) and storage term (long-dashed blue lines) averaged over the analysis domain for selected precipitation periods. Units are mm d^{-1}. Time is UTC.

Figures 19b and 19c display the variation in the vertical profile of the vertical velocity and Q_1 averaged over the period between 09Z 20 May and 15Z 20 May when a strong squall line resided over the experiment domain. It is seen that the strength of vertical motion and diabatic heating is just proportional to the precipitation rates used in the analysis. Larger precipitation rates lead to stronger ascending motion and greater diabatic heating. Generally, the precipitation uncertainty does not affect the level of maximum heating and the general structure of Q_1. It is worth noting that the uncertainty in precipitation could change the sign of the large-scale forcing and diabatic heating when they are weak. For example, the vertical velocity can change from a moderate upward motion to a weak downward motion at levels below 715 hPa with the decrease of precipitation rates for the 20 May case. Similar feature is also seen in Q_1.

5.2. Variation of Budget Structure With Domain Size

To examine how the heat and moisture budgets change with the size of analysis domain, additional analyses were performed over two smaller domains, i.e., Doman B and Domain C as shown in Figure 1a. The observed surface and TOA fluxes averaged over the respective domains are used as the constraints in the variational analysis. Therefore, the variations of budget structure shown below are due to changes not only in domain size but also in these surface constraints. This should be bore in mind in the discussion below. It should be also noted that the analysis over Domain C is largely dependent on the background fields from RUC analyses since its analysis grids are far distant from the boundary sounding stations. By adjusting the atmospheric state variables from RUC analyses to balance the observed column budgets of mass, heat, and moisture, *Xie et al*. [2004a] showed that the quality of the derived budget terms could be significantly improved.

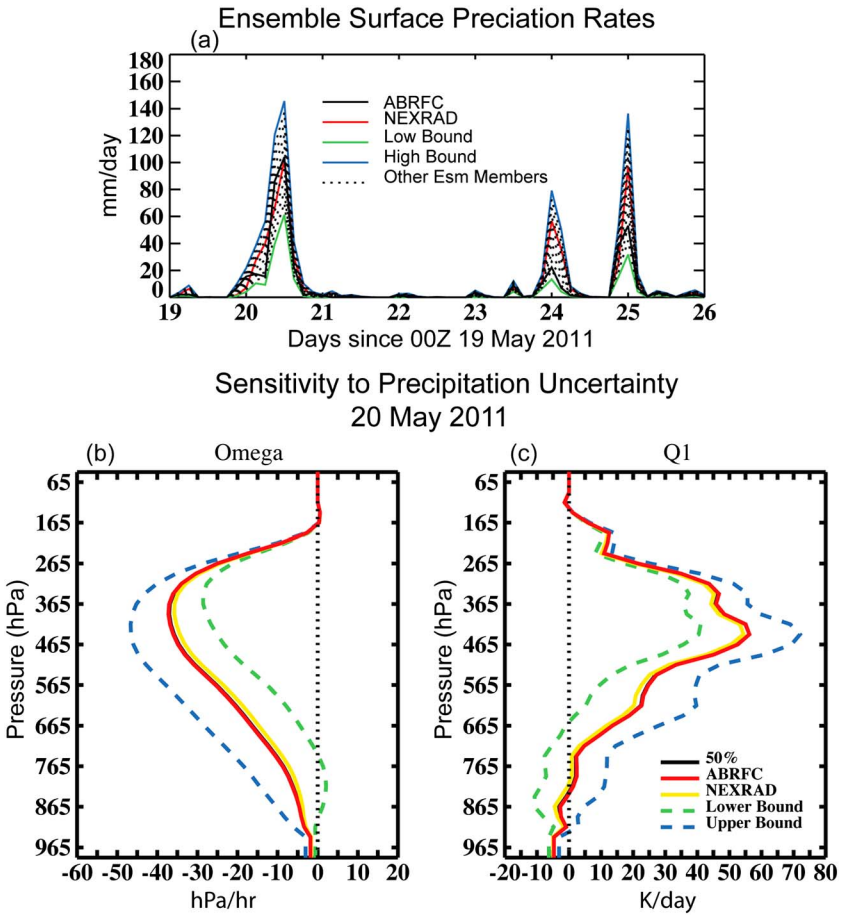

Figure 19. (a) Precipitation ensembles used in the analysis for a selected period of MC3E. Units are mm d^{-1}. (b) Selected ensemble members of analyzed vertical velocity (hPa hr^{-1}) and (c) Q_1 (K d^{-1}) averaged for the period between 09 Z and 15Z 20 May 2011 when a strong squall line propagated the experiment site.

Figure 20a compares the mean precipitation rates over Domains A, B, and C for the same period as that shown in Figure 19a. Differences are seen in the intensity and timing of these precipitation events as the analysis domain size changes, reflecting the large spatial variability in precipitation.

Figures 20b and 20c, respectively, display the variation in the vertical structure of the vertical motion and Q_1 averaged over the same period as that in Figures 19b and 19c. Similarly, larger precipitation rates correspond to stronger upward motion and greater diabatic heating. The vertical structure of the vertical velocity and Q_1 is similar over the three analysis domains except for the level of maximum upward motion over the smallest domain, which is slightly lower than that over the bigger domains. This may be because of a few stratiform clouds contained in the smallest domain as indicated in Figure 20c, in which the secondary peak around 340 hPa in Q_1 over Domain C is not as clear as that shown over the two bigger domains.

6. Summary and Discussion

We have performed a budget analysis to understand interactions between cumulus convection and its environment in the midlatitudes with data collected from the recent field MC3E campaign that was conducted from 22 April to 6 June 2011 at the ARM SGP site. Our analysis has been focused on the variations of the structures in elevated thunderstorms and deeper convective events, two bulk types of convective systems that are often observed in the late spring and early summer in this region. A constrained objective variational analysis approach, which uses surface and TOA flux observations as the constraints, was used to derive the large-scale state structures and Q_1 and Q_2 profiles from the MC3E sounding array. The analyzed fields correspond well with the ARM radar measurements of cloud frequency of occurrence, which

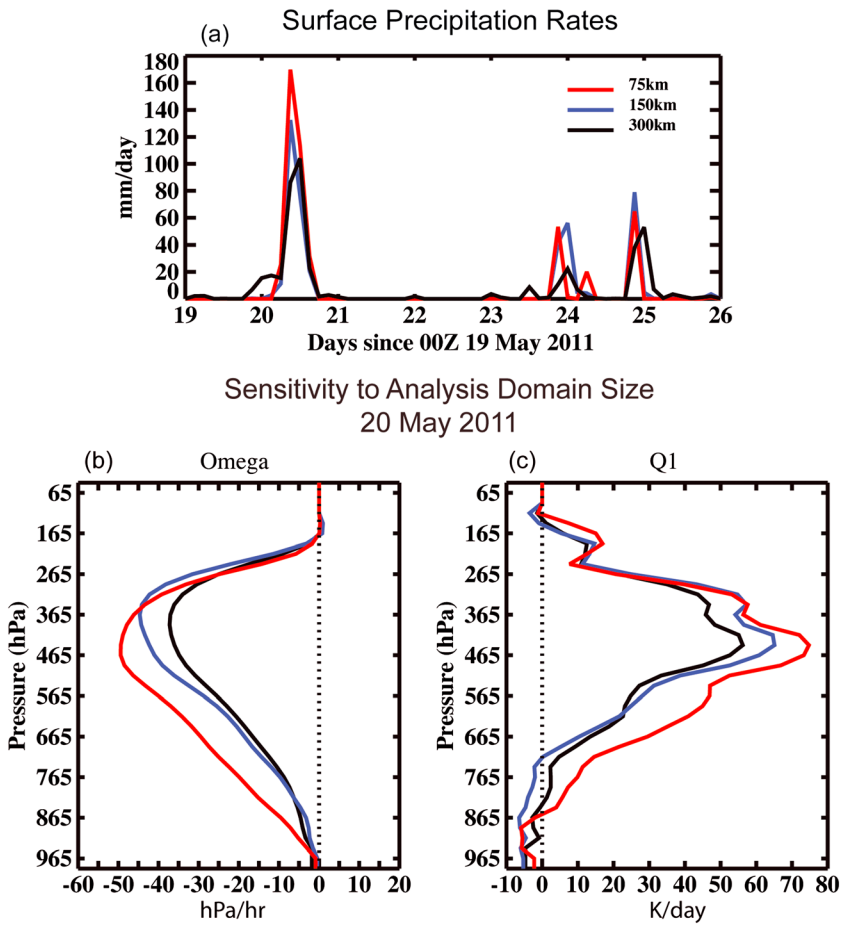

Figure 20. (a) Precipitation rates over different sizes of domain for a selected period of MC3E. Units are mm d^{-1}. (b) Analyzed vertical velocity (hPa h^{-1}) and (c) Q_1 (K d^{-1}) over the three different sizes of domain averaged for the period between 09 Z and 15Z 20 May 2011 when a strong squall line propagated the experiment site.

were not assimilated into the analysis. This provides an independent check on the diagnosed heat and moisture budgets.

Distinct large-scale structures and diabatic heating and drying profiles were found with the two types of convective systems. The examined elevated events were nocturnal precipitation cases. These events initiated in an environment with little CAPE identified from the soundings and were consistent with a very dry boundary layer. Convection in these systems is thought to be initiated at midlevels partially as a result of cloud-radiation interactions in additional to synoptic forcings. Longwave cooling at the top of high stratiform clouds and warming below destabilized the atmospheric column at midlevels. Deep convection eventually occurred from the boundary layer as the systems evolved with time. This top-down destabilization process for nocturnal convection at SGP has been tested in *Lee et al*. [2010] through a cloud-resolving modeling study. The current analysis has provided observational evidence that supports such a hypothesis.

In contrast, the later May supercell and squall lines developed in the morning or early afternoon. Their preenvironments were associated with a large amount of CAPE along with a near-saturated boundary layer. The latter was largely due to the persistent near-surface southeasterlies that brought in sufficient warm and moist air return to the experiment region from the Gulf of Mexico. Very strong deep convection occurred rapidly with its roots in the boundary layer.

As the convective systems reached their maturity, the diabatic heating mainly from latent heat release was much stronger and extended much higher in the squall line type events than in the elevated systems. The level of maximum heating was located at around 340 hPa in the organized deep convection, while it was around 515 hPa in the elevated storms. Accordingly, the upward motion in the squall line type events was

much stronger and reached much higher altitudes than that in the earlier MC3E events. For example, the primary peak of the upward motion was located at around 365 hPa in later May events as compared to 515 hPa in the earlier April and May events. It is worth noting that the Q_1 profile in both types of convection exhibited a considerable cooling in the lower troposphere, which is not often seen in convective systems over tropical oceans. This unique feature in Q_1 associated with midlatitude convective systems has been also found in previous budget studies in this region. It is presumably due to the evaporation of precipitation and low-level clouds.

The diabatic drying in the elevated convective storms was primarily located in the middle troposphere. Below 865 hPa, a considerable moistening was found. This further suggests the existence of the evaporation of precipitation and clouds at low levels. In contrast, the diabatic drying in the deeper convective cells was located mainly in the lower troposphere, reflecting activities of low-level clouds and strong turbulent flux exchanges in the boundary layer during the day. The vertical variations of Q_2 resembled the vertical advection of moisture in the middle and upper troposphere where the vertical transport of moisture provided the necessary moisture supply for convection to consume.

Unlike tropical convection, where the horizontal advection of temperature can be neglected, it played an important role in the heat budget of the midlatitude convective systems. The magnitude of the horizontal temperature advection was comparable to that of the diabatic heating and the vertical transport of temperature in both the lower and upper troposphere for these selected convective systems. The horizontal moisture advection played a dominant role in moistening the lower atmosphere, particularly for the squall lines where the southeasterlies provided persistent low-level moisture supply from the Gulf of Mexico to support convection. It has been found that the column-integrated moisture convergence was leading convection in all the selected events, suggesting that the accumulation of moisture provided a favorable condition to initiate these midlatitude convective systems.

Sensitivity tests further indicated that the uncertainty in the surface precipitation mainly affected the magnitude of these analyzed fields rather than the vertical structure. The same is true with the change of the analysis domain size. However, the analysis domain size change might affect the timing and the level of maximum ascending motion and diabatic heating, depending on how these convective systems were captured by the analysis domains.

Different from earlier budget studies, which were often based on a single case [e.g., *Kuo and Anthes*, 1984 and *Gallus and Johnson*, 1991], the current analysis has performed a composite analysis based on multiple cases. These examined convective events were further separated into groupings of elevated thunderstorms and supercell and squall line events to examine similarities and differences between these two typical convective systems that often occur at SGP. The constrained variational analysis method used in the study has improved the quality of the analyzed large-scale structures and diabatic heating and drying profiles by enforcing the column integral of the analyzed mass, heat, and moisture to be balanced with the surface and TOA observations. Nevertheless, the number of cases studied in the current study is still far too limited. Given the large variations in the analyzed structures among different convective systems, more cases need to be analyzed in order to make the results statistically robust. The DOE ARM program has conducted more than 20 sounding Intensive Operational Periods at SGP over different seasons in the past 20 years. This allows us to perform a statistical study of various midlatitude convective systems over different seasons. This will be our future work.

Convective events that occur at SGP are often associated with west-east propagating mesoscale convective systems. This poses a challenge in studying the relationship between the environment observed in the sounding array and the convection because the size of current ARM sounding array may not be able to appropriately capture the environment for the entire lifecycle of these propagating mesoscale convective systems. Increase of the size of sounding array to cover bigger area to the west of the ARM SGP site should be considered in future planned major field campaigns.

It is noted that the nocturnal elevated convection over the central United States has gained increased scientific attention in recent years [*Horgan et al*., 2007; *Corfidi et al*., 2008; *Lee et al*., 2010]. Several field campaigns have been targeted to understand what allows convection to initiate in the presence of a stable nocturnal boundary layer, such as the International H_2O Project [*Weckwerth et al*., 2004] that was conducted in 2002 at SGP to improve the understanding and prediction of convective initiation. A recently proposed multiagency field campaign PECAN (Plains Elevated Convection At Night) (http://asr.science.energy.gov/meetings/stm/2013/presentations/PECAN-update.pdf) is specifically aimed to the nocturnal elevated

convection and stable boundary layers. The current study represents one of the efforts toward understanding the mechanisms behind these commonly observed convective systems at SGP and provides useful information to the being planned PECAN field campaign.

Acknowledgments

The authors would like to thank the anonymous referees for their valuable comments that helped to clarify and improve the paper. We thank Paul Ciesielski and Richard Johnson for helpful discussion on the use of sounding data. The observational data were obtained from the ARM program sponsored by the U.S. Department of Energy, Office of Science, Office of Biological and Environmental Research, Environmental Sciences Division. Work at LLNL was supported by the DOE ARM program and performed under the auspices of the U.S. Department of Energy by Lawrence Livermore National Laboratory under contract DE-AC52-07NA27344. Work at Stony Brook University was supported by the DOE ASR program. Contributions from Brookhaven National Laboratory were supported by the DOE Atmospheric Systems Research under contract DE-AC02-98CH10886. The data can be obtained from the ARM archive (http://iop.archive.arm.gov/arm-iop/0eval-data/xie/scm-forcing/iop_at_sgp/MC3E/).

References

Barnes, S. L. (1964), A technique for maximizing details in numerical map analysis, *J. Appl. Meteorol.*, *3*, 396–409.

Clothiaux, E. E., T. P. Ackerman, G. G. Mace, K. P. Moran, R. T. Marchand, M. Miller, and B. E. Martner (2000), Objective determination of cloud heights and radar reflectivities using a combination of active remote sensors at the ARM CART sites, *J. Appl. Meteorol.*, *39*, 645–665.

Corfidi, S. F., S. J. Corfidi, and D. M. Schultz (2008), Elevated convection and castellanus: Ambiguities, significance, and questions, *Weather Forecasting*, *23*, 1280–1303, doi:10.1175/2008WAF2222118.1.

Cressman, G. P. (1959), An operational objective analysis scheme, *Mon. Weather Rev.*, *87*, 367–374.

Frank, W. M. (1978), The life cycle of GATE convective systems, *J. Atmos. Sci.*, *35*, 1256–1264.

Frank, W. M., and J. L. McBride (1989), The vertical distribution of heating in AMEX and GATE cloud clusters, *J. Atmos. Sci.*, *46*, 3464–3478.

Gallus, W. A., and R. H. Johnson (1991), Heat and moisture budgets of an intense midlatitude squall line, *J. Atmos. Sci.*, *48*, 122–146.

Gallus, W. A., Jr., and R. H. Johnson (1995), The dynamics of circulations within the trailing stratiform regions of squall lines. Part I: The 10–11 June PRE-STORM system, *J. Atmos. Sci.*, *52*, 2161–2187, doi:10.1175/1520-0469(1995)052<2161:TDOCWT>2.0.CO;2.

Ghan, S., et al. (2000), An intercomparison of single column model simulations of summertime midlatitude continental convection, *J. Geophys. Res.*, *105*, 2091–2121, doi:10.1029/1999JD900971.

Giangrande, S. E., S. Collis, J. Straka, A. Protat, C. Williams, and S. Krueger (2013), A summary of convective-core vertical velocity properties using ARM UHF wind profilers in Oklahoma, *J. Appl. Meteorol. Climatol.*, *52*, 2278–2295.

Giangrande, S. E., S. Collis, A. K. Theisen, and A. Tokay (2014), Precipitation estimation from the ARM distributed radar network during the MC3E campaign, *J. Appl. Meteorol. Climatol.*, doi:10.1175/JAMC-D-13-0321.1.

Hopper, L. J., Jr., and C. Schumacher (2009), Baroclinicity influences on storm divergence and stratiform rain: Subtropical upper-level disturbances, *Mon. Weather Rev.*, *137*, 1338–1357.

Hopper, L. J., Jr., and C. Schumacher (2011), Modeled and observed variations in storm divergence and stratiform rain production in Southeastern Texas, *J. Atmos. Sci.*, *69*, 1159–1181.

Horgan, K. L., D. M. Schultz, J. E. Hales Jr., S. F. Corfidi, and R. H. Johns (2007), A five-year climatology of elevated severe convective storms in the United States east of the Rocky Mountains, *Weather Forecasting*, *22*, 1031–1044, doi:10.1175/WAF1032.1.

Jensen, M. J., T. Toto, D. Troyan, P. E. Ciesielski, D. Holdridge, J. Kyrouac, and J. Schatz (2014), The Midlatitude Continental Convective Clouds Experiment (MC3E) sounding network: Operations, processing and analysis, *Atmos. Meas. Tech. Discuss.*, *7*, 9275–9315, www.atmos-meas-tech-discuss.net/7/9275/2014/, doi:10.5194/amtd-7-9275-2014.

Jensen, M. P., et al. (2010), Midlatitude Continental Convective Clouds Experiment (MC3E), DOE/SC-ARM/10-0004.

Johnson, R. H., and P. E. Ciesielski (2013), Structure and properties of Madden–Julian Oscillations deduced from DYNAMO sounding arrays, *J. Atmos. Sci.*, *70*, 3157–3179.

Johnson, R. H., T. M. Rickenbach, S. A. Rutledge, P. E. Ciesielski, and W. H. Shubert (1999), Trimodal characteristics of tropical convection, *J. Clim.*, *12*, 2397–2418.

Kollias, P., E. E. Clothiaux, M. A. Miller, E. P. Luke, K. L. Johnson, K. P. Moran, K. B. Widener, and B. A. Albrechet (2007), The atmospheric radiation measurement program cloud profiling radars: Second-generation sampling strategies, processing, and cloud data products, *J. Atmos. Oceanic Technol.*, *24*, doi:10.1175/JTECH2033.1.

Kuo, Y.-H., and R. A. Anthes (1984), Mesoscale budgets of heat and moisture in a convective system over the central United States, *Mon. Weather Rev.*, *112*, 1482–1497.

Lee, M.-I., I. Choi, W. Tao, S. D. Schubert, and I.-S. Kang (2010), Mechanisms of diurnal precipitation over the US Great Plains: A cloud resolving model perspective, *Clim. Dyn.*, *34*, 419–437, doi:10.1007/s00382-009-0531-x.

Lewis, J. M. (1975), Test of Ogura-Cho model on a prefrontal squall line case, *Mon. Weather Rev.*, *103*, 764–778.

Lin, X., and R. H. Johnson (1996a), Kinematic and thermodynamic characteristics of the flow over the Western Pacific Warm pool during TOGA COARE, *J. Atmos. Sci.*, *53*, 695–715.

Lin, X., and R. H. Johnson (1996b), Heating, moistening, and rainfall over the western pacific warm pool during TOGA COARE, *J. Atmos. Sci.*, *53*, 3367–3383.

May, P. T., J. H. Mather, G. Vaughan, C. Jakob, G. M. McFarquhar, K. N. Brown, and G. G. Mace (2008), The tropical warm pool international cloud experiment, *Bull. Am. Meteorol. Soc.*, *89*, 629–645.

Milosevich, L. M., H. Vomel, D. N. Whiteman, and T. Leblanc (2009), Accuracy assessment and correction of Viasala RS92 radiosonde water vapor measurements, *J. Geophys. Res.*, *114*, D11303, doi:10.1029/2008JD011565.

Ninomiya, K. (1971), Dynamical analysis of outflow from tornado-producing thunderstorms as revealed by ATS III pictures, *J. Appl. Meteorol.*, *10*, 275–294.

Ooyama, K. V. (1987), Scale-controlled objective analysis, *Mon. Weather Rev.*, *115*, 2479–2506, doi:10.1175/1520-0493(1987)115<2479:SCOA>2.0.CO;2.

Randall, D. A., Harshvardhan, and D. A. Dazlich (1991), Diurnal variability of the hydrological cycle in a general circulation model, *J. Atmos. Sci.*, *48*, 40–62.

Riehl, H., and J. S. Malkus (1958), On the heat balance in the equatorial trough zone, *Geophysica*, *6*, 503–538.

Ryzhkov, A. V., S. E. Giangrande, and T. J. Schuur (2005), Rainfall estimation with a polarimetric prototype of WSR-88D, *J. Appl. Meteorol.*, *44*, 502–515.

Schumacher, C., M. H. Zhang, and P. E. Ciesielski (2007), Heating structures of the TRMM field campaigns, *J. Atmos. Sci.*, *64*, 2593–2610.

Stensrud, D. J. (1996), Effects of persistent, midlatitude mesoscale regions of convection on the large-scale environment during the warm season, *J. Atmos. Sci.*, *53*, 3503–3527.

Thompson, R. M., S. W. Payne, E. E. Recker, and R. J. Reed (1979), Structure and properties of synoptic-scale wave disturbances in the intertropical convergence zone of the eastern Atlantic, *J. Atmos. Sci.*, *36*, 53–72.

Webster, P. J., and R. Lukas (1992), TOGA COARE: The coupled ocean-atmosphere response experiment, *Bull. Am. Meteorol. Soc.*, *73*, 1377–1416.

Webster, P. J., and G. L. Stephens (1980), Tropical upper-tropospheric extended clouds: Inferences from winter MONEX, *J. Atmos. Sci.*, *37*, 1521–1541.

Weckwerth, T., et al. (2004), An overview of the International H2O Project (IHOP_2002) and some preliminary highlights, *Bull. Am. Meteorol. Soc.*, *85*, 253–277.

Xie, S., and M. Zhang (2000), Impact of the convection triggering function on single-column model simulations, *J. Geophys. Res.*, *105*, 14,983–14,996, doi:10.1029/2000JD900170.

Xie, S., et al. (2002), Intercomparison and evaluation of cumulus parameterization under summertime midlatitude continental conditions, *Q. J. R. Meteorol. Soc.*, *128*, 1095–1136.

Xie, S., R. T. Cederwall, and M. Zhang (2004a), Developing long-term single-column model/cloud system-resolving model forcing data using numerical weather prediction products constrained by surface and top of the atmosphere observations, *J. Geophys. Res.*, *109*, D001104, doi:10.1029/2003JD004045.

Xie, S., M. H. Zhang, J. S. Boyle, R. T. Cederwall, G. L. Potter, and W. Y. Lin (2004b), Impact of a revised convective triggering mechanism on CAM2 model simulations: Results from short-range weather forecasts, *J. Geophys. Res.*, *109*, D14102, doi:10.1029/2004JD004692.

Xie, S., et al. (2005), Simulations of midlatitude frontal clouds by SCMs and CSRMs during the ARM March 2000 cloud IOP, *J. Geophys. Res.*, *110*, D15S03, doi:10.1029/2004JD005119.

Xie, S., S. A. Klein, M. Zhang, J. J. Yio, R. T. Cederwall, and R. McCoy (2006), Developing large-scale forcing data for single-column model and cloud-resolving model from the Mixed-Phase Arctic Cloud Experiment, *J. Geophys. Res.*, *111*, D19104, doi:10.1029/2005JD006950.

Xie, S., T. Hume, C. Jakob, S. A. Klein, R. B. McCoy, and M. Zhang (2010a), Observed large-scale structures and diabatic heating and drying profiles during TWP-ICE, *J. Clim.*, *23*, 57–79, doi:10.1175/2009JCLI3071.1.

Xie, S., et al. (2010b), CLOUDS AND MORE: ARM climate modeling best estimate data, *Bull. Am. Meteorol. Soc.*, *91*, 13–20, doi:10.1175/2009BAMS2891.1.

Xu, K.-M., et al. (2002), An intercomparison of cloud-resolving models with the ARM summer 1997 IOP data, *Q. J. R. Meteorol. Soc.*, *128*, 593–624.

Xu, K.-M., et al. (2005), Modeling springtime shallow and deep frontal clouds with CRMs and SCMs, *J. Geophys. Res.*, *110*, D15S04, doi:10.1029/2004JD005153.

Yanai, M. (1961), A detailed analysis of typhoon formation, *J. Meteorol. Soc. Jpn.*, *39*, 187–214.

Yanai, M., and R. Johnson (1993), Impacts of cumulus convection on thermodynamic fields, *Meteorol. Monogr.*, *46*, 39–62.

Yanai, M., S. Esbensen, and J. Chu (1973), Determination of bulk properties of tropical cloud clusters from large-scale heat and moisture budgets, *J. Atmos. Sci.*, *30*, 611–627.

Young, C. B., A. A. Bradley, W. F. Krajewski, A. Kruger, and M. L. Morrissey (2000), Evaluating NEXRAD multisensor precipitation estimates for operational hydrologic forecasting, *J. Hydrometeor.*, *1*, 241–254, doi:10.1175/1525-7541(2000)001<0241:ENMPEF>2.0.CO;2.

Zhang, C., J. Gottschalck, E. D. Maloney, M. W. Moncrieff, F. Vitart, D. E. Waliser, B. Wang, and M. C. Wheeler (2013), Cracking the MJO nut, *Geophys. Res. Lett.*, *40*, 1223–1230, doi:10.1002/grl.50244.

Zhang, J., K. Howard, and J. J. Gourley (2005), Constructing three-dimensional multiple-radar reflectivity mosaics: Examples of convective storms and stratiform rain echoes, *J. Atmos. Oceanic Technol.*, *22*, 30–42, doi:10.1175/JTECH-1689.1.

Zhang, M. H., and J. L. Lin (1997), Constrained variational analysis of sounding data bases on column-integrated budgets of mass, heat, moisture, and momentum: Approach and application to ARM measurements, *J. Atmos. Sci.*, *54*, 1503–1524.

Zhang, M. H., J. L. Lin, R. T. Cederwall, J. J. Yio, and S. C. Xie (2001), Objective analysis of ARM IOP Data: Method and sensitivity, *Mon. Weather Rev.*, *129*, 295–311.